SIQI SONG

Master Thesis

Feasibility of locally-coupled elasto-plastic damage modeling for remaining life prediction of low-speed damaged roller bearings under heavy loading condition

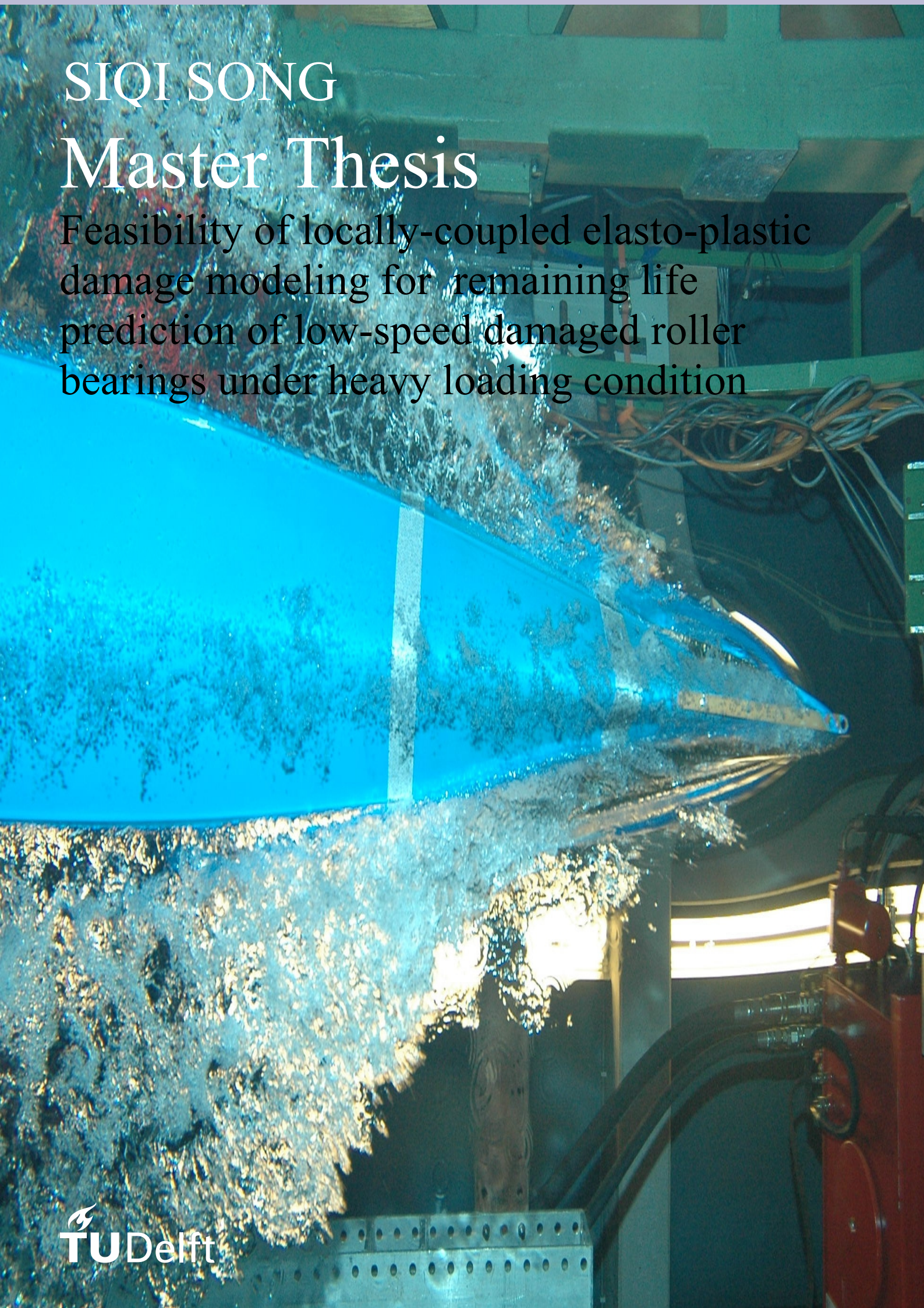

TU Delft

Master Thesis

Feasibility of locally-coupled elasto-plastic damage modeling for remaining life prediction of low-speed damaged roller bearings under heavy loading condition

by

SIQI SONG

to obtain the degree of Master of Science
at the Delft University of Technology,
to be defended publicly on Friday May 28, 2021 at 10:00 AM.

Project duration:	April 21, 2020 – April 21, 2021	
Thesis committee:	Dr. L. Pahlavan,	TU Delft, supervisor (chair)
	Dr. C. Walters,	TU Delft
	Dr. H. den Besten,	TU Delft
	Ir. B. Scheeren,	TU Delft, daily supervisor

TU Delft

Contents

Preface

The whole year of this research is dynamic and fantastic, which is more like League of Legends or Arena Of Valor. The main question in my research is the inhibitor, meanwhile, the sub-questions are the turrets. I thought my role in the research is like the mage in Arena of Valor and at least rated as gold level. Every issue encountered in this research appears to act as an enemy hiding in the grass, however, the mage is always being attacked inadvertently. No matter how fierce the attack is, the mage will try her best to face it. Sometimes the choice of the graduation topic is really like the different modes of the game called Undertale. Deadline is like the monster to chase people at the Temple running.

No matter in the research or the game, team spirit is essential. Mage without support cannot reach the inhibitor at the end. The first person I want to thanks is my supervisor Pooria who gave me such an interesting research topic and supported me in a lot of aspects. My English listening is still been improved, and he always slows down his voice so that I can follow the discussions. What's more, I also learned a lot about academic writing skills from his detailed comments. Another person I want to thank is my daily supervisor Bart for all the guidance he gave me. Without these two people, I cannot finish this research. Additionally, Carey is also the person I sincerely want to thanks for his detailed comments and questions, which helped me a lot!

Other people I want to thank are my friends who helped me to pass through such a tough time under covid. I remember the days that we communicate under social distance. The last I want to thank is my families who always encourage me to do what I want and act as big back stones for me. Whatever I meet, when I look back or want to have a rest, my families are still there to support me and give me space to relax.

Wish you like this thesis!

There are more methods than difficulties .
SIQI SONG
China, May 2021

Abstract

Low-speed roller bearings are generally in the sheave bearings and turret bearings which are used in the offshore industry under heavy loads. One of the challenges to the integrity of these bearings is the presence of subsurface cracking in the raceways. Downtime cost, which is caused by the failure of these bearings is significant. Based on the potential of the recently-developed monitoring methods for detection of damage in low-speed bearings, this research is focused on the feasibility of the remaining lifetime prediction for roller bearings with existing subsurface cracking in the raceways.

The main approach of this thesis comprises a locally-coupled elasto-plastic damage model for low-cycle fatigue. In the numerical simulations, models with and without crack have been implemented and subjected to heavy loading condition. To avoid the crack singularity in the FEM, and reduce the mesh sensitivity, a non-local method has been applied to determine the strain data around the crack tip. In a post-processing part, the nonlinear damage accumulation is implemented with a multi-yield surfaces algorithm.

To assess and validate the computational accuracy, the implemented locally-coupled elasto-plastic damage model has been compared with other (published) results. The numerical simulations suggest that the number of cycles to failure is about two times higher when the detectable crack size decreases from 20mm to 5mm. From these results, it is recommended to improve the monitoring system for the detection of smaller cracks. Moreover, further experimental assessment is required to validate and update the estimations in the thesis.

List of Abbreviations

Abbreviation	Indicating
AE	Acoustic Emission
CH	Chaboche hardening
CHRI	Chaboche kinematic hardening rate independent
EHL	Elastohydrodynamic lubrication
FEA	Finite element analysis
FEM	Finite element method
FPSO	Floating production storage and offloading
RCF	Rolling contact fatigue
RO	Ramberg-Osgood
RVE	Representative Volume Element
SPM	Single Point Mooring
XFEM	Extended finite element method

List of Symbols

The next list describes several symbols that will be later used within the body of the document.

Greek symbols	Usage
α	Localisation parameter
β	Localisation parameter
$\gamma^{(1),(2),(3)}$	Rates of kinematic hardening in Chaboche kinematic hardening material model
ν	Poisson's ratio
Δ	Amplitude
δ	Kronecker delta
σ	Stress state
σ_{eq}	Equivalent stress
σ_i	i^{th}yield stress
σ_{i+1}	$i+1^{th}$ yield stress
σ_{xx}	Stress at xx direction
σ_{xy}	Stress at xy direction
σ_{yy}	Stress at yy direction
σ_m	Hydrostatic stress
σ_{max}^{*}	Maximum damage equivalent stress
$\sigma_{max}^{initial}$	Initial maximum damage equivalent stress
σ_{max}^{last}	Last maximum damage equivalent stress
σ_{ij}^{M}	Stress tensor at the micro scale
σ_{xy}	Stress at xy direction
σ_{yy}	Stress at yy direction
σ_y	Yield stress
τ	Shear stress
$\dot{\lambda}$	Plastic multiplier
ε	Strain tensor
ε_{ij}^{tot}	Total strain tensor
ε_{ij}^{e}	Elastic strain tensor
ε_{ij}^{p}	Plastic strain tensor
ε_{xx}	Strain at xx direction
ε_{xy}	Strain at xy direction
ε_{yy}	Strain at yy direction
ε^{p}	Plastic strain
ε_{i}^{p}	i^{th} plastic strain
ε_{i+1}^{p}	$i+1^{th}$ plastic strain
ε_{ij}^{MP}	Plastic strain tensor at the micro scale
$\dot{\varepsilon}_{ij}^{p}$	Plastic strain increment tensor
ε	Strain in pseudo-undamaged state
$\tilde{\varepsilon}$	Effective strain at damaged state

Latin symbols	Usage
A	Pseudo-undamaged area
A_D	Damaged area
a	Crack length
C_{ijkl}	Elastic modulus tensor
D	Damage variable
$\dot{D}$	Damage increment with time interval
d	Distance of center of yield surface shifts
D_c	Threshold of damage
d	Crack depth
E	Elastic modulus
e	Distance between crack center and center of contact area
E_0	Elastic modulus at the undamaged state
e_{ij}^e	Deviatoric elastic strain tensor
e_{ij}^p	Deviatoric plastic strain tensor
e^p	Deviatoric plastic strain
F	Yield function
F_i	Yield function at the i^{th} yield surface
F_{i+1}	Yield function at the $i+1^{th}$ yield surface
G	Shear modulus
h	Distance between crack front and center of contact area
K'	Cyclic strength coefficient in Ramber-Osgood material model
k	Scale factor in multi yield surface algorithm
$\vec{n}$	Normal vector
n'	Cyclic strain hardening exponent in Ramber-Osgood material model
p	Positive root of the yield function
$\dot{p}$	Equivalent plastic strain increment with time interval
p	Equivalent plastic strain
R	Radii in stress state
R_∞	Limit of isotropic hardening
r	Radii in stress-strain curve
S	Damage strength
S_{ij}	Devatoric stress tensor
s	Damage exponent
S_x	Deviatoric stress at xx direction
S_y	Deviatoric stress at yy direction
W^e	Elastic strain energy density
$X_\infty^{(1),(2),(3)}$	Back stress components in Chaboche kinematic material model
X_i	Back stress at the i^{th} yield surface
X_{i+1}	Back stress at the $i+1^{th}$ yield surface
X_{ij}	Back stress tensor

List of Figures

List of Tables

1

Introduction

In the offshore industry, performance of machinery and equipment degrades with time, which can lead to decreased production efficiency, reduced safety, and even complete failure. Low-speed roller bearings are one of the fundamental components in the offshore machinery. A common approach is to replace damaged bearings. Based on this aspect, when to replace these bearings is of special concern to the operators because of the costs associated with downtime. One of the industrial desires is to predict the remaining lifetime of roller bearings based on condition monitoring. This research is aimed to evaluate the feasibility of the remaining lifetime prediction for roller bearing running below 60rpm (revolution-per-minute) based on the monitoring results and damage modeling [1].

1.1. Roller bearings in offshore applications

Generally, a roller bearing has four basic components: outer raceway, inner raceway, roller, and cage. A schematic of roller bearing is illustrated in figure 1.1. The outer raceway is normally the fixed part and support rollers; the inner raceway is mounted on a shaft. Rollers ride between the inner and outer raceways. The cage reduces friction and wear by preventing contact between rollers [44].

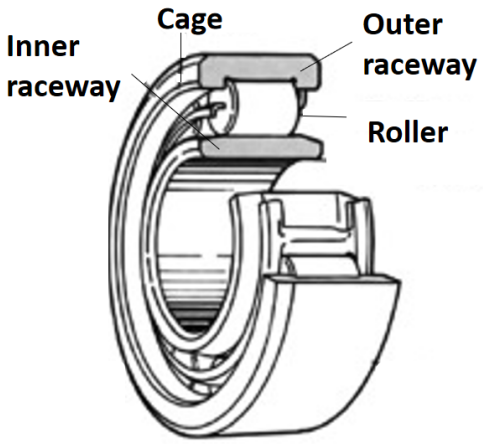

Figure 1.1: Basic components of roller bearing [44]

Low-speed roller bearings are widely used in the offshore industry such as sheave bearings and slew bearings in the offshore heavy-lift vessels, turret bearings of floating production storage and offloading

[1] Note that 0-60rpm is the part of the “low-speed range”. However, this ”low-speed range” is generally referred to 0-600rpm, even though a clear cut between low-speed and high-speed has not been well established [47].

(FPSO) vessels, main shaft bearing in the wind turbine. Sheave bearings in offshore vessels and turret bearings of FPSO vessels are mainly considered in this section.

Sheave bearings are normally under heavy loading, both radially (from the load itself) and axially. They can take enormous loads while moving at a slow rotational speed because of the micro motions of the ship [23]. A case of sheave used in a flex-lay system of Huisman is shown in the figure 1.2.

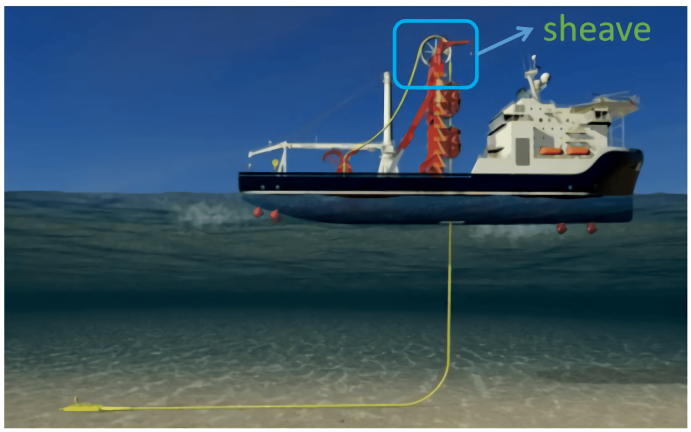

Figure 1.2: Sheave in the Flex-lay system of Huisman [8]

Low-speed roller bearings are commonly designed in the turret system of FPSO vessels. As seen in figure 1.3, in a Single Point Mooring (SPM) system, the turret system usually has two main bearing systems: the upper major bearing and the lower bearing. The upper bearing is normally the key load bearing, which takes all the axial loads and the weight of the turret, while the lower bearing is generally configured to take mainly radial loads [29].

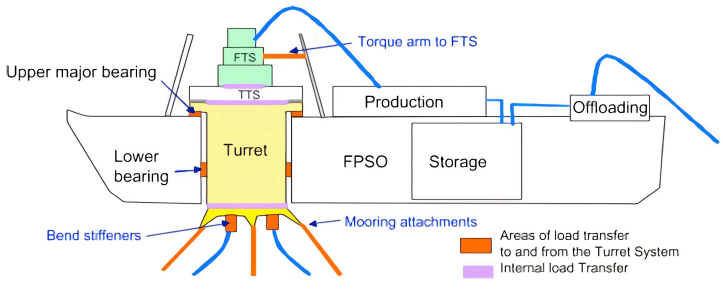

Figure 1.3: A simple section scheme of a FPSO vessels with a turret system [27]

1.2. Typical damage in low-speed roller bearings

In offshore general operations, these bearings are usually exposed to a harsh environment such as corrosive salt water, temperature fluctuations, and external wave and wind loading, which can initiate and enhance the degradation of the bearings. If a damaged bearing goes undiagnosed, and is not replaced in time, secondary damage to the machine and its components can develop and result in catastrophic failure [19]. It can be difficult, to determine the root cause of the failure [19]. Roller bearings exhibit six main modes of damages [36]:

1. Spalling originated from subsurface cracking.
2. Core crushing occurred in the surface hardened material.
3. Pitting initiated on the surface.
4. Origin at local concentrations of pressure (roller ends, etc).
5. Peeling which is also called ‘micro pitting’.

6. Section fracture.

Among these failures, two main modes are dominant in roller bearing failure: surface originated pitting and subsurface originated spalling. Figure 1.4 shows two typical cracks due to pitting and spalling. These two phenomena commonly can act separately. Pitting originates from the free surface and develops to the subsurface (see figure 1.4 (a)) while spalling approaches from subsurface to the free surface (see figure 1.4 (b)). However, they may also interfere in the growth stage and cooperate to fail the material. In general, pitting can be visible on the surface and hence hindered by employing better lubricants and more efficient lubrication techniques, but there are not actually many ways to stop spalling once initiated during the operation of the bearing. Therefore, it is important to understand the mechanisms leading to spalling as a result of subsurface cracking to improve the bearing lifetime estimation [32].

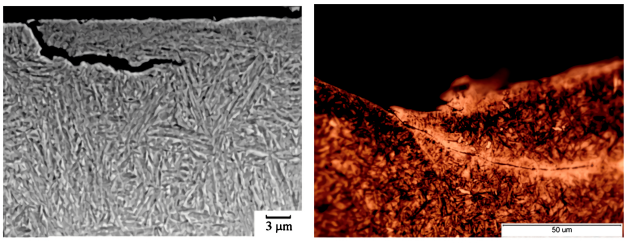

(a) (b)

Figure 1.4: Failure due to surface pitting (a) as opposed to subsurface spalling (b) [32]

1.3. Importance of lifetime prediction

In the offshore industry, low-speed heavily-loaded roller bearings are theoretically designed for a lifetime of decades. But these bearings in harsh offshore environment can in practice be at a potential failed state earlier than the expected time. These low-speed roller bearings are produced by only a few suppliers and are often custom-built, resulting in the replacement being time-consuming and leading to operation down-time, which can also be very costly [29]. Therefore, a prediction of the remaining life of these damaged roller bearing is important.

1.4. Background

1.4.1. Rolling contact fatigue versus structural fatigue

Rolling contact fatigue is one of the main fatigue degradation types and is considered different from structural fatigue. The most notable differences are listed below [16]:

- The state of stress in non-conformal contact which is present in rolling contact fatigue is complex and multiaxial. The stress calculation in ball/roller bearing is governed by the Hertzian point/line contact within elastic limit. As for classical fatigue, unaxial state is usually considered.

- The loading history at the subsurface point is non-proportional as illustrated in figure 1.5 . In this figure, the stress history is shown for a subsurface point is at the depth where the orthogonal shear stress τ_{xz} is maximum. Normal stresses σ_x and σ_z are always compressive while the shear stress τ_{xz} remains a complete reversal. The peaks of both normal stresses are not in accordance with the peaks for the shear stress.

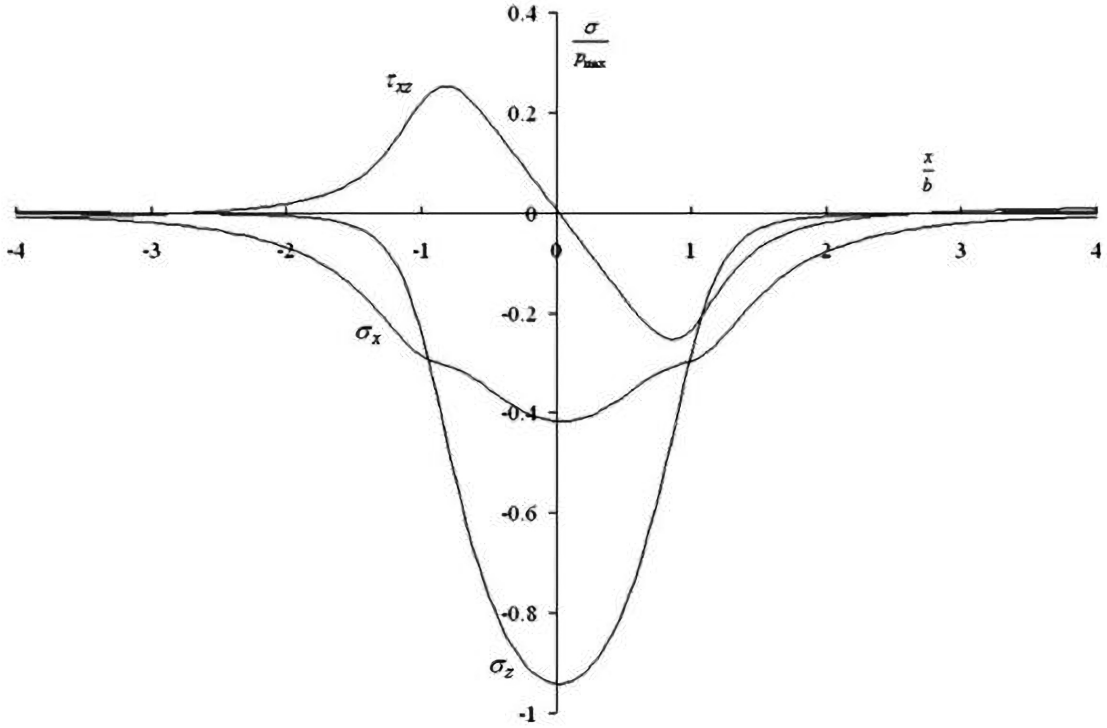

Figure 1.5: Stress history at a subsurface point in a Hertzian line contact [16]

- The principal axes constantly change in direction during a stress cycle due to which the planes of maximum shear stress also change.

- It is difficult to identify the planes where maximum fatigue damage occurs for rolling contact fatigue.

- High hydrostatic stress component occurs in the non-conformal contact, which is less pronounced in tension- compression or bending fatigue.

- The phenomenon of rolling contact fatigue (RCF) occurs in a very small volume of stressed material, because the contact stress field is highly localized.

1.4.2. Mechanism of spalling

Subsurface cracks generally originate at the material inhomogeneities such as non-metallic inclusions or at the location of the maximum shear stress and propagate toward the surface to form surface spalling [16].

Before branching toward the surface, subsurface cracks normally propagate a long way, which determine the sudden de-attachment of large portion of material with potentially consequent catastrophic and unexpected failure [13]. Subsurface cracks often approximately run in parallel to the surface. In some zones, local 'zigzag' patterns are also seen, as illustrated in figure 1.6.

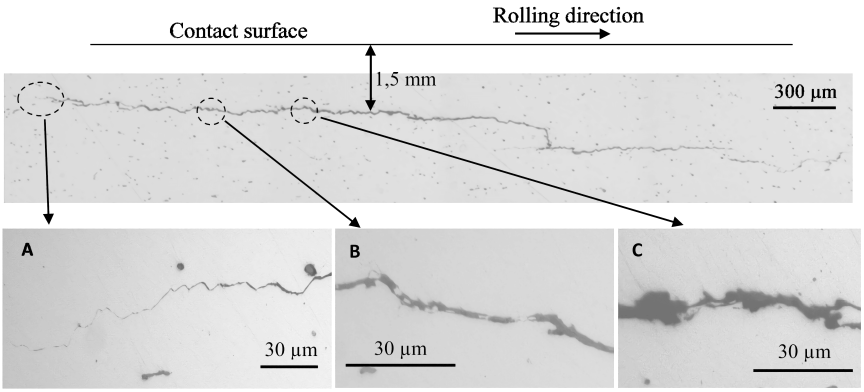

Figure 1.6: Subsurface cracks in raceway at a nominal contact pressure of 2000 MPa for 8.17 $\times 10^5$ cycles [13]

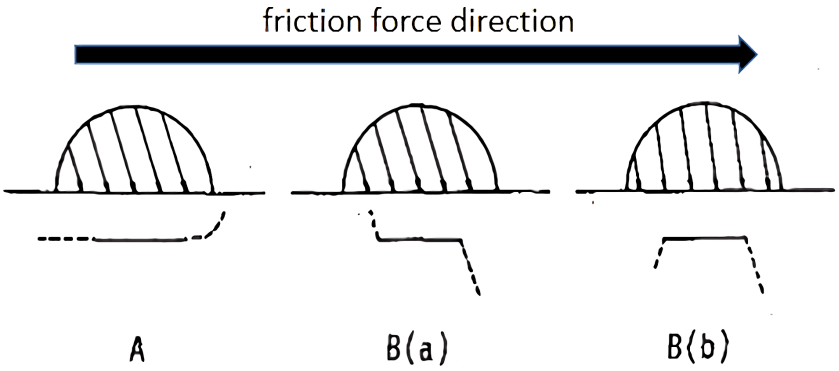

Figure 1.7: Direction of crack growth in 2D plane (A: Mode II growth; B: Mode I growth ((a) high surface friction, (b) low surface friction) [21].The solid line represent the present crack, the dash line denote the potential direction of crack growth. The friction force at the free surface is opposite to the the roller movement. The hemispheres with hatches represent Hertz contact pressure.

For elastic material, crack growth behaviour in Hertzian contact also depends on different surface frictions, which is demonstrated in figure 1.7. As can be seen in figure 1.7, the direction of subsurface crack growth is different for the left and the right tips of the crack with respect to the direction and magnitude of the surface friction [21].

Due to globally compressive stress under rolling contact area, the closure effect prevents the cracks from opening. The stress field on the crack is schematically in the figure 1.8.

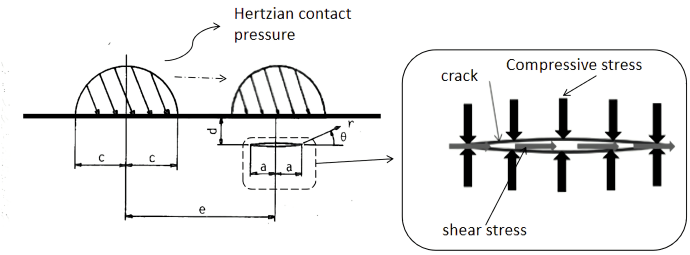

Figure 1.8: Schematic view of stress field on the subsurface crack within 2D-half infinite plane [21]. As shear stress orientate left, crack may grow in left-horizontal direction.

For elasto-plastic materials, the irreversible nature of plastic flow contributes to the mechanism of subsurface crack growth. At the beginning, the crack propagation is driven mainly by the local plastic strains around crack tip [3]. The resulting permanent deformation due to plastic strain zone may keep parts of the crack, or even the entire crack, open [43]. This also means that mode I crack growth should not be ignored because of plastic deformation. As further rolling contact cycling occurs, these small cracks either branch or coalesce with other cracks to form a dominant crack [3]. When the crack reaches a certain length, its path changes from parallel to inclined and eventually reaches the surface forming a spall [3], as illustrated in figure 1.9.

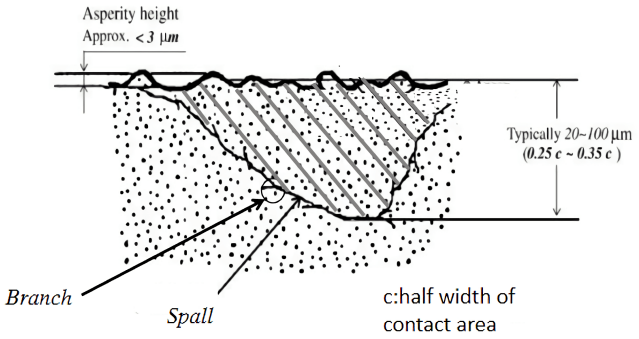

Figure 1.9: Schematic view of spall [46]. The shadow area with the hatched part is the potential disappearing part due to spalling.

1.4.3. Damage mechanism

Damage is the deterioration which occurs in materials prior to failure [24]. The damage accumulation is described by Miner's linear accumulation theory which means that a structure fails when damage amounts to 1 [20]. The limitation of this method is that the rate of damage accumulation is independent of the stress level, which is not true in ductile fatigue. Additionally, if this method is used for life prediction under random loading conditions, it is recommended to use it with Monte Carlo simulation. The equation 1.1 is written as follows:

$$D = \sum_{i=1}^{k} \frac{n_i}{N_i} \leq 1 \tag{1.1}$$

Where: n_i is the number of cycles accumulated in the i^{th} block of constant amplitude loading. N_i is the average number of cycles to failure at i^{th} block of constant amplitude loading. k is the total blocks of constant amplitude loading. $D \leq 1$ is applicable in the load sequence of stress level varying from high to low [38].

To describe this deterioration to failure in multiaxial fatigue, damage can broadly be defined as an isotropic scalar variable D (which is bounded by 0 (undamaged state) and 1 (totally damaged state)) [24]. This simple definition of damage is to describe damage as the ratio of damaged area and pseudo-undamaged area in a one-dimensional case of homogeneous volume element. As illustrated in figure 1.10, the effective stress is then defined by the cross sectional area reduction in the damaged state:

$$D = \frac{A_D}{A} \rightarrow \tilde{\sigma} = \frac{F}{A - A_D} = \frac{\sigma}{1 - D}, \tilde{\varepsilon} = \varepsilon \tag{1.2}$$

Where: A_D is the damaged area. A is the pseudo-undamaged area. ε is the strain in pseudo-undamaged state. $\tilde{\varepsilon}$ is the effective strain at damaged state. $\tilde{\sigma}$ is the effect stress at damaged state. σ is the stress at pseudo-undamaged state.

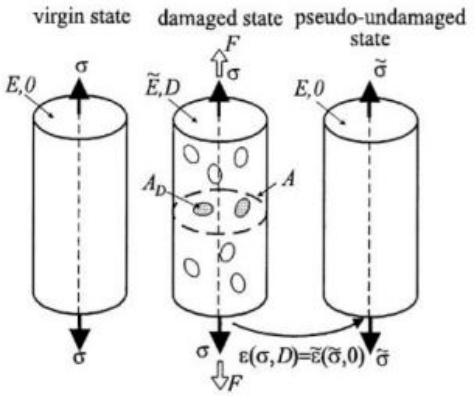

Figure 1.10: Illustration of one-dimensional damaged element [24]. $\varepsilon(\sigma, D) = \varepsilon(\sigma, 0)$ means that the strain is the same within both damage state or pseudo-undamaged state.

As illustrated in the figure 1.10, such one dimensional element is called as Representative Volume Element (RVE). The mechanical state of the continuum is unique on condition that the RVE is the statistical representation of the actual material. For experimental purposes and numerical analysis, it is useful to consider the magnitude of the Representative Volume Element and this maximum scale for metal is recommended as 0.1 mm^3 [24].

During this deterioration, the damage evolution can be divided into three main parts: initiation (Stage I), growth (Stage II) and fracture (Stage III), which are depicted in figure 1.11.

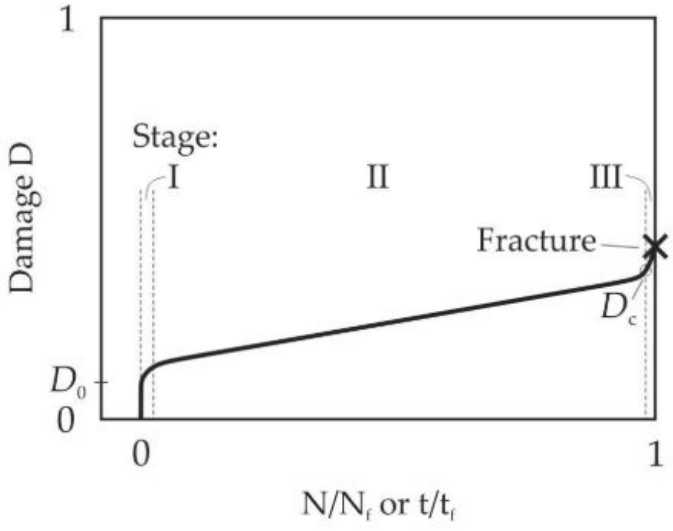

Figure 1.11: Schematic of a typical damage development during static and cyclic tests (Mean stress/strain is 0) [12].

In low cycle fatigue, ductility is assumed dominant in fatigue. This means that low cycle fatigue can be described as growth of ductile damage, which results from the nucleation of cavities and the matrix followed by their growth and their coalescence through the phenomenon of plastic instability. Based on this aspect, the degrees of localization of ductile damage is comparable to that of plastic strain [24]. In general, local plasticity increment cause a permanent decrease in stiffness matrix. In other words, as a result of crack growth, the damage variable (D) is described in terms of stiffness loss [12]. In practise,

the damage variable (D) can be measured by the variation of elastic modulus [24]:

$$D = 1 - \frac{E}{E_0} \tag{1.3}$$

Where: E_0 is the modulus with undamaged state.

To describe the damage accumulation in quantification, a nonlinear damage law is introduced in equation 1.4, which models damage growth governed by plasticity (through the plastic strain increment $\dot{p}$) [10]. Within one load cycle, the damage growth rate can be rewritten as follows:

$$\dot{D} = \left(\frac{Y}{S}\right)^s \dot{p} \tag{1.4}$$

Where: S is the damage strength, which is obtained by material testing. s is the damage exponent, which is also obtained by material testing. Furthermore, this value is assumed as 1 in mental [24]. Y is the energy release rate. $\dot{p}$ is the equivalent plastic strain increment with time interval. $\dot{D}$ is the damage increment with time interval.

$$\frac{dD}{dN} = \int_{1\text{ cycle}} \dot{D}dt \approx \left(\frac{(\sigma^*_{\max})^2}{2ES}\right)^s \int_{1\text{ cycle}} \dot{p}dt \tag{1.5}$$

1.4.4. Locally-coupled method

Depending upon the level at which the effects of damage on the strain behaviour of the material are taken into account, three approaches are list [24]: uncoupled, locally-coupled, fully-coupled.

The main steps of uncoupled approach are listed as follows:

1. Structural calculation to obtain the stress/strain field has no direct relationship with the damage mechanism. This step is simulated by FEM.
2. Find the potential damaged area from the structural calculation.
3. Introduce the stress and plastic strain at the potential damaged area into the damage evolution law.

Locally-coupled approach is illustrated as follows:

1. Structural calculation has no direct relationship with the damage mechanism. This step is simulated by FEM.
2. Find the potential point from the structural calculation.
3. The strains obtained by step 2 is used to integrate the fully-coupled strain damage constitutive equations locally.

Fully-coupled approach in one step: strain-damage coupled constitutive equations are solved by FEM.

Accuracy is sorted from high to low: fully-coupled > locally-coupled > uncoupled. Meanwhile, time computation is sorted from high to low: fully-coupled > locally-coupled > uncoupled.

For localized damage, locally-coupled approach is a good method, which performs the coupling only by solving a set of differential equations. When the fully-coupled analysis is applied, the constitutive model is only calculated on a single Gaussian integration point, and the calculated result is called by the unit, and then the overall stiffness matrix is assembled and solved by the solver. This method can give a higher accuracy but it also needs more computation time. In the heavily-loaded condition, the convergence can be a numerical challenge due to the complexity of non-linear contact issue and large deformation caused by the heavy load. Considering that the accuracy of locally-coupled method is lower than fully-coupled approach, the calculated lifetime based on locally-coupled method is to be viewed as an estimate. The damage mechanism is only included in the fatigue analysis in the locally-coupled approach. Since it is only applied analytically after the FEA results are obtained, the calculation procedure is often considered as an analytical solution.

Strictly speaking, the locally-coupled method described in [24] is focused on the micro scale under the assumption of the Lin-Taylor strain compatibility hypothesis, which states that the state of strain at the micro scale is equal to the state of strain at the meso scale as derived from the classical structural calculation [24]. As the FEM results are in the meso scale, this assumption can cause large underestimation of lifetime when the locally-coupled method is applied in high cycle fatigue regime. Luckily, in low cycle regime, the estimation is acceptable [41]. In high cycle regime or the transition regime between low cycle and high cycle regime, the Eshelby-Kröner localization law of micro mechanics is applied to transform meso scale to micro scale which is shown as follows [41]:

$$\sigma_{ij}^{M} = \sigma_{ij} - \alpha E \varepsilon_{ij}^{Mp} \tag{1.6}$$

Where: σ_{ij}^{M} is the stress tensor at the micro scale. σ_{ij} is the stress tensor at the meso scale. ε_{ij}^{Mp} is the plastic strain tensor at the micro scale. α and β are the localisation parameter which are given by:

$$\alpha = \frac{1-\beta}{1+\nu}, \quad \beta = \frac{2(4-5\nu)}{15(1-\nu)} \tag{1.7}$$

Where: ν is the Poisson's ratio.

1.4.5. Cyclic plasticity in material

As discussed in the former section, plasticity plays a dominant role in low cycle fatigue. In rolling contact condition, plasticity also has large influence on the contact area, and reduces the peak value of the contact pressure because of the increasing conformity of the two contacting bodies and reduced height of the raceway surface due to plastic deformation [14]. Therefore, to investigate the damage evolution in a periodic loading condition within roller bearing, a proper cyclic plasticity model should be considered into material. This section will discuss the main principles of the cyclic plasticity model.

Plasticity requires the definition of a yield function, a flow rule, a hardening law [39].

The yield condition is represented by a convex surface in the stress space [2]. A stress space is established by using the stress magnitude as the measure of distance along the coordinate axis [2]. In the case of perfect plastic materials, this surface will remain unchanged after the yield stress is reached. However, if strain-hardening is considered, the yield surface will change in line with the hardening rule for the values of stress beyond the initial yield point, where the yield point will rise to the new value of the stress state in the strain-hardened material.In metals, it is common to define the Von Mises yield condition in terms of the deviatoric stresses, assuming that the hydro-static stress has negligible effect on the plastic deformation [2]. An illustration of yield conditions is shown in figure 1.12. This figure also shows that the yield condition is independent of hydro-static stresses. A Von Mises equivalent stress σ_{eq} is calculated by equation 1.8 to predict yielding of materials under multiaxial loading conditions.

$$\sigma_{eq} = \sigma_y = \sqrt{\frac{3}{2} S_{ij} S_{ij}} \tag{1.8}$$

Where: S_{ij} is the deviatoric stress.

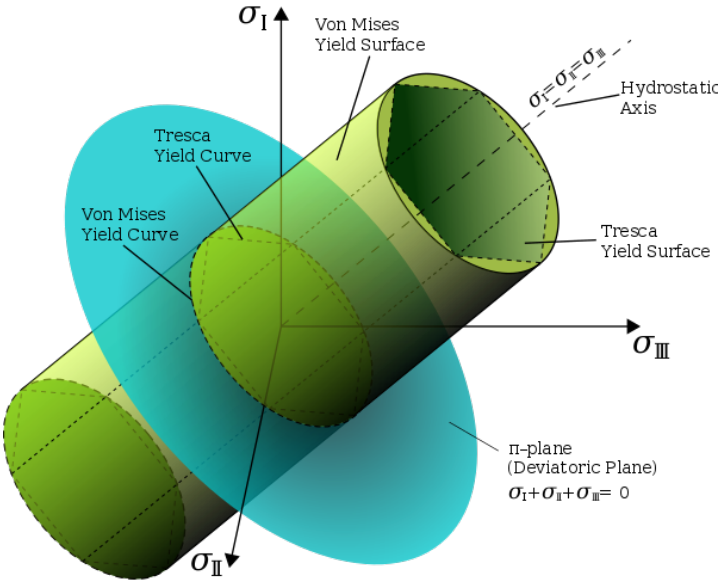

Figure 1.12: The Von Mises yield conditions in principal stress coordinates circumscribes a cylinder with radius $\sqrt{\frac{2}{3}}\sigma_y$ around the hydrostatic axis. Also shown are Tresca's hexagonal yield surface .σ_y is the tensile yield strength of the material. [42]

Flow rule gives the ratio or relative magnitude of the components of the plastic strain increment tensor, as well as defines its corresponding direction in the strain space [2]. The total strain tensor ε_{ij}^{tot} is generally assumed as the sum of plastic strain tensor ε_{ij}^{p} and elastic strain tensor ε_{ij}^{e} [40], such as:

$$\varepsilon_{ij}^{tot} = \varepsilon_{ij}^{e} + \varepsilon_{ij}^{p} \tag{1.9}$$

After the elastic limit is reached, the state of stress lies on the yield surface. If loading continues, hardening can be manifested in one of these two (or both) forms: isotropic or kinematic. The following is the summary of basic information about these two forms:

- The kinematic hardening related to the state of the internal micro-stress concentration. The related back stress describes the shifting of the center of the elastic domain in tension/compression (or in three dimensions) [24] , see figure 1.13 (a).
- The isotropic hardening model relates to the density of dislocations or flow arrest [24] and expands the yield surface of a material under plastic deformation [2], see the figure 1.13 (b).

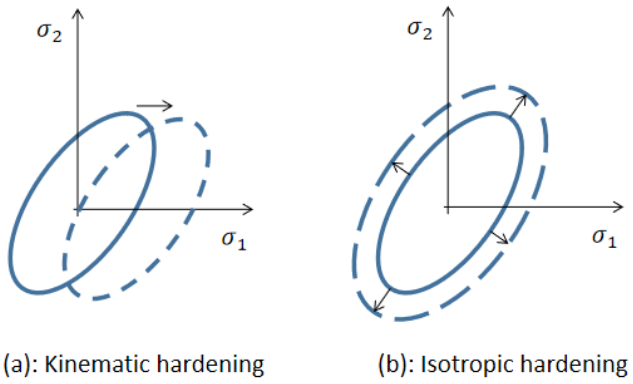

Figure 1.13: Kinematic hardening (a) vs Isotropic hardening (b)

In order to compute the damage accumulation in one cycle, the appropriate stress-strain constitutive relations of the material should be considered. Firstly, the material is assumed to be homogeneous (no

non-metallic inclusions) and isotropic. Its response is considered isothermal, which means the energy release rate is only produced by plasticity work, and no heat transform. Thus the Young's modulus of elasticity and the elastic Poisson's ratio are assumed to be constant [18]. In non-proportional loading, the stress-strain response is dependent on the loading history [31]. The stress-strain relationship coupled with damage within elastic limit is rewritten as follows:

$$\sigma_{ij} = (1 - D)C_{ijkl}\varepsilon^e_{ij} \tag{1.10}$$

Where: σ_{ij} is the stress tensor at different directions. ε^e_{ij} is the elastic strain at the different directions. C_{ijkl} is the elasticity modulus tensor.

The stress can be divided into two parts: devatoric (S_{ij}) and hydrostatic state (σ_m), as illustrated in equation 1.11.

$$S_{ij} = \sigma_{ij} - \sigma_m\delta_{ij} \tag{1.11}$$

Where: σ_m is the hydrostatic stress, which is the average of the three normal stress components. δ_{ij} is Kronecker delta, $\delta_{ij} = 1$ if $i = j, \delta_{ij} = 0$ if $i \neq j$.

In a simple way, the deviatoric stress can be rewritten as follows [31]:

$$S_{ij} = 2Ge^e_{ij} \tag{1.12}$$

Where: e^e_{ij} is the deviatoric part of ε^e_{ij}. G is shear modulus.

Since plasticity is the material behaviour when the stresses exceed the yield limit, yield surface, flow rule, and hardening rules are also discussed here.

The yield surface is defined in the stress space as the convex surface between elastic and plastic regions [2]. When damage is small, plasticity is dominant, the material exhibits (isotropic/kinematic) hardening, and the yield surface is typically convex. But as damage is accumulated, the material experiences softening, which may cause the stiffness matrix to change from symmetric to asymmetric and even the values in stiffness matrix can become negative. In the unstable state, different material have different behaviours. In this thesis, 42CrMo4 follows isotropic softening and kinematic hardening rules [37]. This behaviour causes the intersection between yield surfaces. As the unstable state is normally occurs in the first several cycles and can add difficulty in the fatigue estimation, the unstable state is ignored in this thesis. As the yield surface in stress state may shrink into a cone, trial stress in radial return method cannot go back to the yield surfaces. In other words, the convergence can not be assured. For these reasons, the multi-yield surfaces within incremental plasticity method is applied in this thesis instead of backward Euler method with radial return method.

The plasticity is normally affected by the deviatoric part of stresses [31]. As illustrated in figure 1.14, Von Mises criterion in deviatoric stress state is a circle. Furthermore, the use of circles instead of the ellipses greatly simplifies the calculation of incremental plasticity without consideration of whether the yield surface is convex or not.

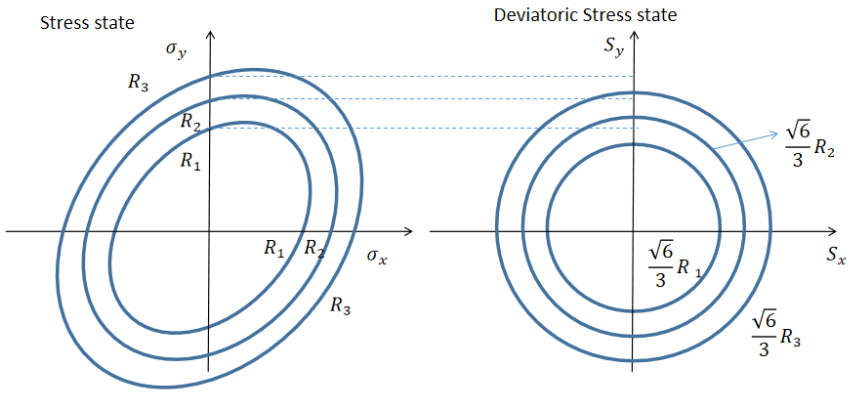

Figure 1.14: Von Mises yield surface in the $\sigma_x - \sigma_y$ stress space (left) and in the $S_x - S_y$ stress space (right) in 2D, when back stress $X_{ij} = 0$. [31]

The yield function coupled with back stress is also convenient to calculate in Von Mises criterion (see equation 1.13).

$$F = \tilde{\sigma}_{\mathrm{eq}} - R = 0$$
$$\tilde{\sigma}_{\mathrm{eq}} = \frac{\sqrt{\frac{3}{2}(S_{ij}-X_{ij})(S_{ij}-X_{ij})}}{(1-D)}, \tag{1.13}$$

Where: $\tilde{\sigma}_{\mathrm{eq}}$ is the equivalent stress coupled with damage. X_{ij} is the back stress.

For metals, it is convenient to assume that plasticity potential equals to the yield function. For this reason, the plastic strain increment can be written as follows:

$$\dot{\varepsilon}_{ij}^{p} = \dot{\lambda}\frac{\partial g}{\partial \sigma_{ij}} = \dot{\lambda}\frac{\partial F}{\partial \sigma_{ij}} \tag{1.14}$$

Where: g is plastic potential. $\dot{\lambda}$ is plastic multiplier and this value is non-negative.

Equation1.14 also assumes that the plastic strain increment vector is normal to the yield surface (as indicated in the figure1.15), and the direction is $\frac{\partial F}{\partial \sigma_{ij}}$. Hence the plastic increment is deviatoric (see equation 1.16), the normal vector ($\vec{n}$) can be rewritten as follows in the equation 1.15:

$$\vec{n} = \frac{\partial \mathrm{F}/\partial \sigma_{ij}}{|\partial \mathrm{F}/\partial \sigma_{ij}|} = \frac{\partial \mathrm{F}/\partial \mathrm{S}_{ij}}{|\partial \mathrm{F}/\partial \mathrm{S}_{ij}|} \tag{1.15}$$

$$de^{p} = d\varepsilon^{p} \tag{1.16}$$

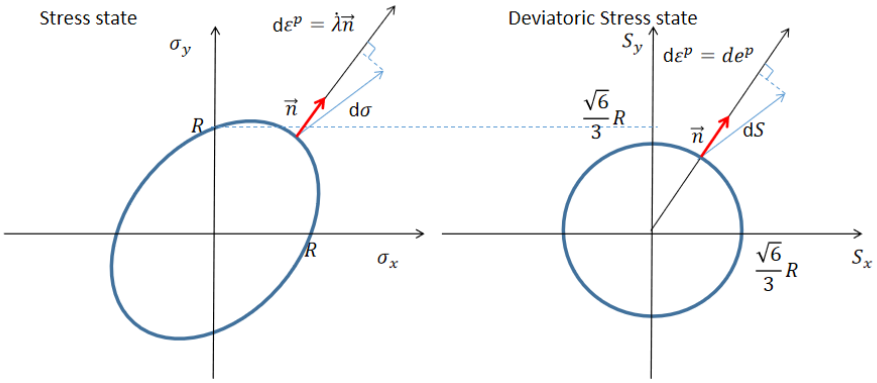

Figure 1.15: Normal vector on the Von Mises yield surface in the $\sigma_x - \sigma_y$ stress space (left) and in the $S_x - S_y$ stress space (right) in 2D, When back stress $X_{ij} = 0$ [31].

As illustrated in figure 1.15, when yield function $F(S_{ij}, R) < 0$, the stress increment is purely elastic. But if σ lie on the yield surfaces and its variation $\dot{\sigma}$ is in the outward direction of yield surface ($\dot{F} > 0$), the plastic strain increment should be put into consideration. Normally, for those perfectly plastic material, according to the equation 1.14, the plastic increment is explicitly calculated since the plastic multiplier can be directly derived from the consistency condition ($\dot{F} = 0$). For nonlinear elastoplastic materials, this method is not accurate and can cause overestimation in fatigue life prediction. Normally, the plastic increment can be calculated by the hardening rules, which is shown in equation 1.17:

$$d\varepsilon^{p} = \frac{1}{C_i} \cdot (d\sigma \cdot \vec{n}) \cdot \vec{n} \quad \Rightarrow \quad de^{p} = \frac{1}{C_i} \cdot (dS_{ij} \cdot \vec{n}) \cdot \vec{n} \tag{1.17}$$

Where: C_i is effective plastic modulus at i^{th} yield surfaces (as illustrated in the figure 1.16), which is calculated as follows:

$$C_i = \frac{2}{3} \cdot \frac{d\sigma}{d\varepsilon^{p}} \cong \frac{2}{3} \cdot \frac{\sigma_{i+1} - \sigma_i}{\varepsilon_{i+1}^{p} - \varepsilon_i^{p}} = \frac{2}{3} \cdot \frac{\sqrt{6}}{2} \cdot \frac{r_{i+1} - r_i}{\varepsilon_{i+1}^{p} - \varepsilon_i^{p}}$$

Where: r_{i+1} is the $i+1^{th}$ radii in deviatoric stress state. r_i is the i^{th} radii in the deviatoric stress state, see figure 1.16.

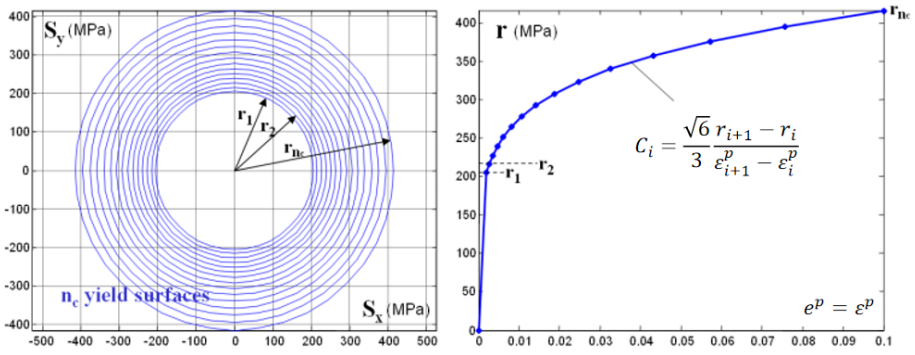

Figure 1.16: Yield surfaces in the $S_x - S_y$ 2D deviatoric stress space, and correspondent radii obtained from the piecewise linearization of the cyclic effective stress-strain curve [31]

Equation 1.17 shows the formula to calculate the plastic strain increment by effective plastic modulus. Under non-proportional loading, as shown in figure 1.16, the nonlinear effective stress-strain curve can be replaced by the piecewise linearization. With sufficiently small segments, the linearization can match well with the nonlinear stress-strain curve.

Under non-proportional loading, the deviatoric stress S_{ij} may move differently from the ring translation direction. Mròz and Garud kinematic hardening rules are normally proposed to describe the translational moment of the yield surface in proportional loading. However, in non-proportional loading, Mròz may cause two yield surfaces intersect and thereby result in numerical error [31].

Figure 1.17 shows the Mròz and Garud kinematic hardening rules in deviatoric stress. Mròz assumes that the translation of yield surfaces is parallel to the line $\overline{SS}_M$. In complex non-proportional loading, the yield surfaces can interact at more than one points resulting in the numerical issue. To avoid this issue, yield surfaces are allowed to be tangent but cannot intersect. When it comes to Garud's rule, it is assumed that the translation of yield surfaces is along the side of the line $\overline{S}_{G'}$ $\overline{S}_G$. In other words, the external normal vector at $\overline{S}_{G'}$ on the i^{th} yield surface remains the same as the one at $\overline{S}_G$ on the $i+1^{th}$ yield surface.

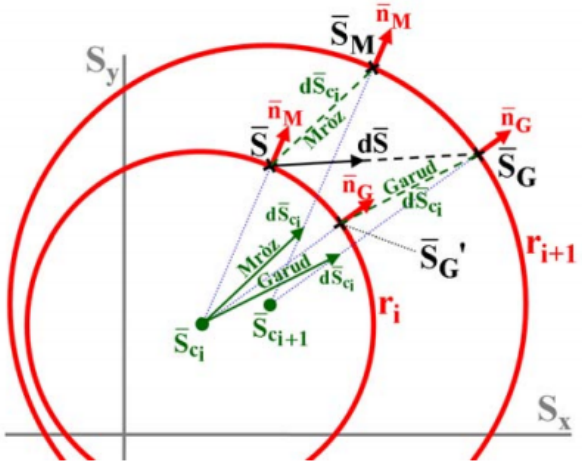

Figure 1.17: Mròz and Garud kinematic hardening rules in deviatoric stress [31].

It is assumed that the size and shape of the yield surfaces do not change. During plastic strain, the

center of the yield surface shifts as following [18]:

$$\Delta X = p\mathbf{d} \tag{1.18}$$

Where: ΔX is the change of back stress in deviatoric stress state. $\mathbf{d}$ is calculated in equation 1.19.

$$\mathbf{d} = (1 - r_i/r_{i+1})\left(S_{ij} - X_{i+1} + k\Delta S_{ij}\right) + (X_{i+1} - X_i) \tag{1.19}$$

The non-negative scalar factor k is calculated by the rewritten yield function [18]:

$$\begin{aligned}&(3/2)\left(S_{ij} - X_{i+1} + k\Delta S_{ij}\right)\cdot\left(S_{ij} - X_{i+1} + k\Delta S_{ij}\right) - r_{i+1}^2 = 0\\ &\text{(i.e., by solving } F_{i+1}\left(S_{ij} + k\Delta s_{ij}, X_{i+1}, r_{i+1}\right) = 0\text{),}\end{aligned} \tag{1.20}$$

p is the positive root of the new written yield function (equation 1.21) [18]:

$$\begin{aligned}&(3/2)\left(S_{ij} + \Delta S_{ij} - X_i - p\mathbf{d}\right)\cdot\left(S + \Delta S_{ij} - X_i - p\mathbf{d}\right) - r_i^2 = 0\\ &\text{(i.e., by solving } F_i\left(S_{ij} + \Delta S_{ij}, X_i + p\mathbf{d}, r_i\right) = 0\text{).}\end{aligned} \tag{1.21}$$

1.4.6. AE monitoring

Condition monitoring of roller bearings is aimed to predict the bearing failure before it happens. These bearings need to be monitored online. The life estimation is also based on the information on the monitored state of the bearing. For roller bearings, subsurface raceway fatigue cracking is of interest in this research.

Since spalling is initiated under surface, it cannot be inspected without stopping the operations and disassembling the bearing. The number of cycles for remaining life of critical length of spalling is also unknown. For this, one primarily needs to know the crack current location, crack size, and the stress or strain field of the potential damaged area. Normally, we can not measure or visibly estimate the serious level of theses defects when the bearings are under the operation condition directly. In practise, there remain some physical variables that can be monitored directly during the operation period. These variables normally can be divided into Acoustic Emission (AE), vibration, temperature, wears in oil and so on [48].

In high-speed bearings, the vibration monitoring (acceleration) is commonly applied, while, in low-speed bearings, the AE method has high efficiency in earlier investigations [7]. Acoustic emission signal analysis methods include parametric analysis and wave analysis. These two analysis methods are used to diagnosis whether there are defects in the bearing and to distinguish the location of defects [25]. For this reason, a structural health monitoring system consists of AE is developed and implemented in the laboratory environment. These measurements can provide information to a damage evolution model which means, the location of crack and the crack size is obtained by passive ultrasonic waves.

AE signals are generated by a rapid release of energy from localized sources within a material and travel through the structure [26]. To measure the crack location, the dominant waveform mode can be identified. Meanwhile, the predefined threshold of signals is set up at the data acquisition system. For those signals crossing over the predefined threshold, the relative arrival time can be extracted. Furthermore, crack source location can be identified through an error minimization problem [26]. The following figure shows the AE parameters in one event. Crack depth and length can be obtained from the wave signals and advanced signal processing techniques [7].

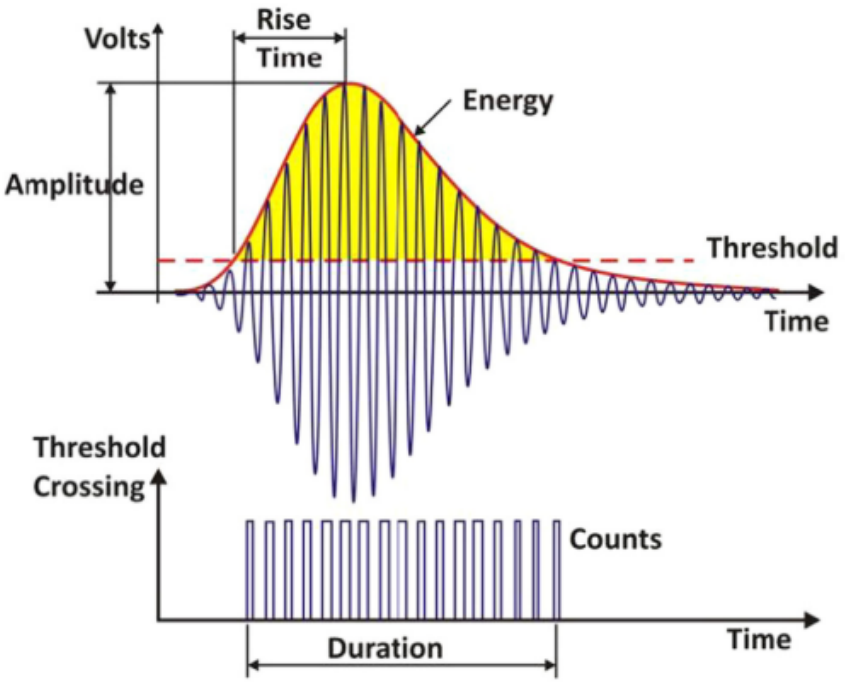

Figure 1.18: AE hit parameters on one event [45].

1.5. Research scope and questions

With the advancement of Acoustic Emission monitoring systems, it has become possible to identify the existing damage state in the low-speed roller bearings [7]. It will be of substantial impact for maintenance decisions if the remaining lifetime of the bearing after detection of damage can also be estimated. This research is focused on the feasibility of the remaining lifetime prediction for roller bearings with existing subsurface cracking in the raceways.

The considered low-speed roller bearings in this research are subjected to heavy loads, which are high enough to cause the localisation of plasticity. Since the bearings have quite low rotational speed ($< 60rpm$), the inertial effect is ignored and quasi-static case is applied. In addition, perfect rolling condition with no friction is considered by fine Elastohydrodynamic lubrication (EHL) condition.

The following is the main question of this research:

> **How to estimate the number of cycles that will take for the raceway to fail under the applied load and with the present damage state?**

The sub-questions can help us to answer the main question:

- How can a damage growth model be implemented based on nonlinear damage evolution method for estimation of the remaining lifetime of the raceway in rolling contact fatigue?
- How can the model take the estimated damage size into account provided by a non-destructive estimation method , e.g. Acoustic Emission monitoring?
- What is the influence of initial crack size and location on the remaining lifetime of the raceway?

1.6. Organization of the thesis

This report is divided into three main chapters based on the former sub-questions organised and two appendices.

Chapter 2, Methodology, consists of the details about FEM and fatigue analysis, which is the core part of this research. It starts with the FEM set-up assuming input from the monitoring results, and followed by fatigue analysis, as a result, the investigation of the remaining lifetime is obtained.

Chapter 3, Results and discussion, provides numerical evaluation of the proposed approach. In this part, the results from FEM simulation and prediction in Matlab are discussed and provided the logical answers to the main questions given in the former section.

Chapter 4, Conclusions and recommendations, highlights the main findings in this research and suggestions for further work.

Appendix A is the validation of the implemented methodology.

Appendix B is the proposed further study which combines the presented approach with Acoustic Emission monitoring tests.

2

Methodology

2.1. Combination of analysis and monitoring

In roller bearings, damages such as subsurface raceway cracks are often invisible and only be detected once spalling occurs and manifests itself as metallic particles in the samples. Considering recent advancements in condition monitoring of low-speed roller bearings, the crack state has been shown to be detectable by Acoustic Emission (AE) method. Based on the AE potential, a new way to estimate the remaining lifetime of bearings is investigated in this thesis.

Considering possible information from AE monitoring, the basic geometry information about crack was set up in FEM, such as crack sizes and common crack depth under surface. Under similar loading condition with laboratory tests by Scheeren et al [7], the strain/stress history around the crack tip was recorded by quasi-static analysis, which simulated the stress/strain field around crack tip at critical locations within one cycle of rolling. Finally, to predict the lifetime range, cyclic plasticity material behaviour is considered into the fatigue analysis. Coupling the damage mechanism with elasto-plastic constitutive equations, the damage accumulation with cycles were obtained.

The figure 2.1 shows the different steps of the method.

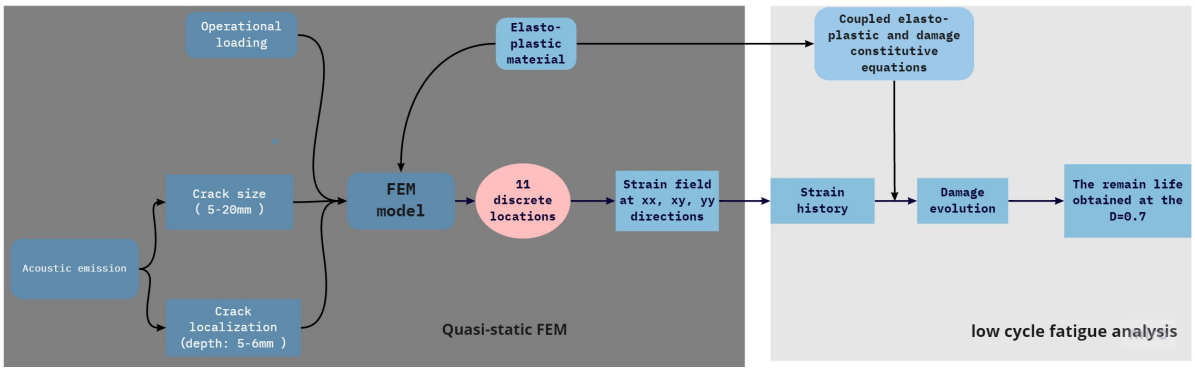

Figure 2.1: Flowchart of the proposed method

2.2. Finite element analysis

The aim of finite element analysis is to reproduce the strain history around crack tip. Considering the changing relative positions of the crack with the respect to the roller during small moment of the bearing, the crack was moved within the contact area to simulate the strain field changes in one cycle of roller passage. Since the contact between each roller and raceway is a line, considering the simulation time, 2D FEM model is used in this thesis. Furthermore, the speed of rolling is low, which means the inertial effects can be also ignored. For this reason, the quasi-static analysis was applied instead of explicit transient analysis. As for quasi-static analysis can not give the complete strain history, 11 discrete locations within the contact influenced area are considered to capture the strain history.

2.2.1. Geometry set up

A 2D FEA model is shown in the figure 2.2. Three rollers and two raceways were considered. Compared with diameter of the rollers (69mm), the gap (2mm) between rollers was small. From this aspect, the neighbour rollers effect on the strain field can not be ignored, which means that the global model should be considered in FEM simulation. The contact type between roller and raceway is a line contact. The reduced cracked raceway model of the size $211mm \times 32.5mm$ is represented by a two-dimensional domain model (figure 2.2). The crack in this model is assumed as a perfect notch. Different subsurface pre-remaining cracks of length varying from $a = 5mm$ to $20mm$ are positioned at the depths between $d = 5mm$ and $d = 6mm$ below the surface. The front crack tip (right side) is placed in 11 positions (e) at the same depth (d), which is also illustrated in figure 2.2. Three rollers and the upper raceway are constrained in the horizontal direction while the bottom raceway is constrained in all directions.

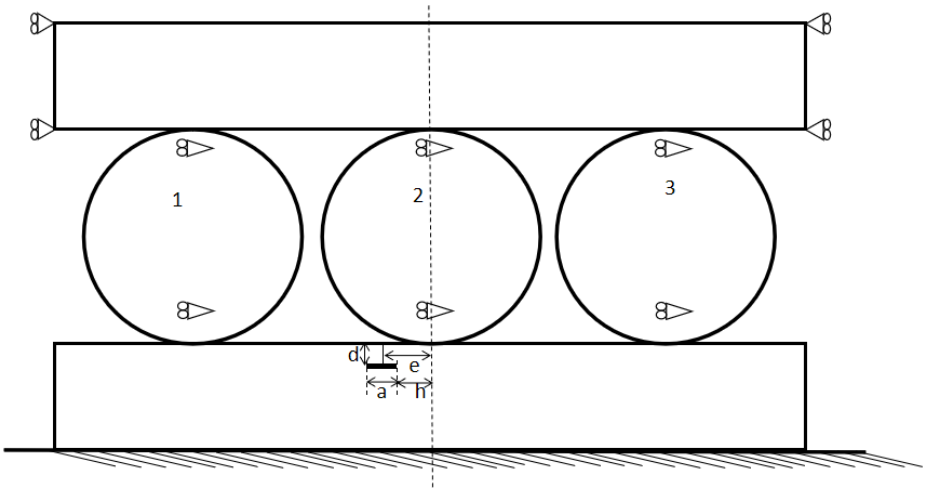

Figure 2.2: Crack positioning in the 2D geometry model. Note that: a is the crack length, e is the distance between crack tip and central line of roller 2 and d is the depth of the crack.

2.2.2. Material choices

An elastic-plastic material model is employed to capture the material behaviour of tempered bearing steel (42CrMo4,296HV) under rolling contact and the constitutive model is coupled with Lemaitre's damage evolution law to capture the material degradation due to low cycle fatigue [4].

According to ref [37] and Ansys material reference [30], kinematic Chaboche hardening plasticity model (CH) is considered in FEM. The material parameters are shown in table 2.2, and it is observed that R_∞ is negative. In other words, the material is considered as isotropic softening from the monotonic state to the stabilized cyclic state. It is acknowledged that the combined behaviors of isotropic softening and kinematic hardening can lead to the interaction of adjacent yield surfaces. However, the method of the multi-yield surface is assumed that the neighboring yield surfaces are tangent. From this aspect, the explicit algorithm based on the multi-yield surfaces simulates this complex condition badly. Since the isotropic softening behavior only occurs in the first few cycles, it is reasonable to omit the isotropic softening behavior [37]. The simple kinematic model (Ramber-Osgood) is considered in the fatigue life estimation, which is shown in the equation 2.1. This equation illustrates the relation between true plastic strain amplitude $\frac{\Delta\varepsilon_p}{2}$ and true stress amplitude $\frac{\Delta\sigma}{2}$. The material parameters are shown in table 2.1.

$$\frac{\Delta\sigma}{2} = K'\left(\frac{\Delta\varepsilon^p}{2}\right)^{n'} \tag{2.1}$$

Where: K' is the cyclic strength coefficient. n' is the cyclic strain hardening exponent.

The cyclic Chaboche kinematic hardening model is writtern as follows [37]:

$$\frac{\Delta\sigma}{2} = \left(R_\infty + \sigma_y\right) + X_\infty^{(1)} \tanh\left(\gamma^{(1)}\frac{\Delta\varepsilon^p}{2}\right) + X_\infty^{(2)} \tanh\left(\gamma^{(2)}\frac{\Delta\varepsilon^p}{2}\right) + X_\infty^{(3)} \tanh\left(\gamma^{(3)}\frac{\Delta\varepsilon^p}{2}\right) \tag{2.2}$$

Where: R_∞ is the limit of isotropic hardening and $R_\infty > 0$ means that the material is isotropic hardening and $R_\infty < 0$ means that the material is isotropic softening. σ_y is the yield strength after stabilised cyclic state. $\gamma^{(1)}, \gamma^{(2)}, \gamma^{(3)}, X_\infty^{(1)}, X_\infty^{(2)}, X_\infty^{(3)}$ are the rates of kinematic hardening and back stress components separately.

Table 2.1: Cyclic material parameters of the damage model for the 42CrMo4 steel in fatigue life estimation [37]

$E(MPa)$	$\sigma_y(MPa)$	ν	K′	n′
198085	620	0.3	1062	0.0866

Table 2.2: Cyclic material parameters of the damage model for the 42CrMo4 steel in FEM [37]

E(MPa)	ν	σ_y (Mpa)	R_∞	$\gamma^{(1)}$	$\gamma^{(2)}$	$\gamma^{(3)}$	$X_\infty^{(1)}$	$X_\infty^{(2)}$	$X_\infty^{(3)}$
198085	0.3	550	-110	60	243	1249	169	117	86

Figure 2.3 shows the comparison of experimental data points and cyclic stress-strain curves calculated with Ramberg-Osgood and Chaboche kinematic rate independent material models for differently heat treated 42CrMo4 steels [37].

Observed from this figure, the difference of Ramberg-Osgood (RO) and Chaboche kinematic hardening rate independent material models (CHRI) is small. From this aspect, it is acceptable to simulate the fatigue life cycle estimation of Ramberg-Osgood model following the FEM results. Meanwhile, both kinematic hardening models match well with the experiments [37].

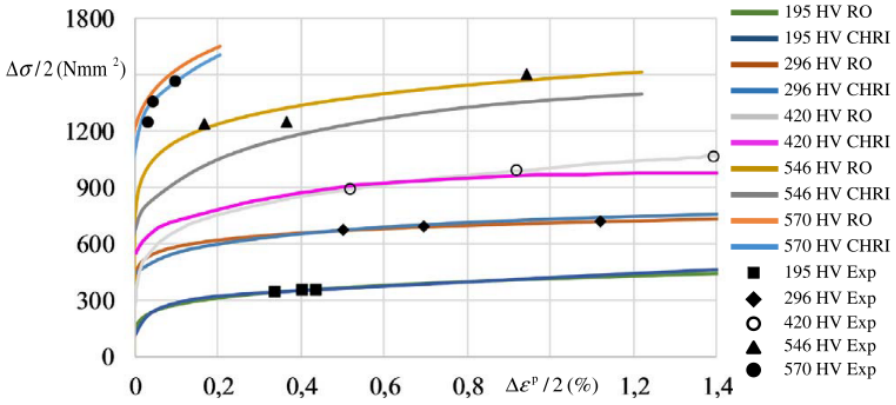

Figure 2.3: Comparison of experimental data points and cyclic stress-strain curves calculated with Ramberg-Osgood (RO) and Chaboche kinematic rate independent material models for differently heat treated 42CrMo4 steels. Note that CHRI means Chaboche hardening rate independent, in other words, isotropic softening is not considered into CHRI model. [37]

2.2.3. Analysis type

Plane strain and plane stress are both approximations of the 3D situation. Since the geometry of the rollers and raceways with crack is uniformed in the out of plane direction and the loading condition is also uniformed along the axis of the rollers, plane strain condition is considered. This dimension reduction of degree of freedom in model will reduce the computational time and also improve the convergence of the model [5].

For the contact algorithm, augmented Lagrange multiplier is chosen instead of penalty method. The contact type is surface to surface.

2.2.4. Element choice

Two main element types in Ansys are discussed here. One is the Plane 182, which is linear element with four nodes [9]. The other one is Plane 183, a quadratic element with 8 nodes or 6 nodes [9]. Both elements are illustrated in figure 2.4 and figure 2.5.

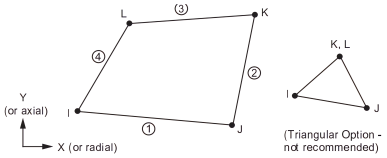

Figure 2.4: Plane 182 [9]

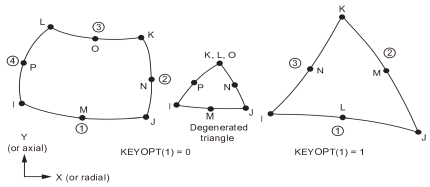

Figure 2.5: Plane 183 [9]

Since the contact analysis is nonlinear, the accuracy of capturing the roller curvature can also influence the results. The quadratic element is expected to perform better than the linear element. Plane 183 is hence chosen.

2.2.5. Crack model

In the conventional FE modelling of cracks, the crack surfaces coincide with the boundaries of the elements. In this context, singularity of the solution at the crack tips is a well-known issue [1, 6, 35, 41]. Mesh refinement and redistribution around the crack tips cannot fundamentally solve the singularity problem. Furthermore, when fully coupling the damage model with FEM, the ill-conditioning issue is intensified at the crack tips resulting in instabilities and spurious bifurcations of the obtained solutions [35]. The root of such issue is that the shape functions in FEM cannot capture the displacement jump at the discontinuity (leading to infinite strains). In addition, complexity of non-linear contact issue and large deformation caused by the heavy load further complicate the convergence of the solution.

The crack is modeled as a slit in this thesis. The locally-coupled method applied (in which the FE model is uncoupled from the damage mechanism) does not suffer from the singularity and convergence issue present in the fully-coupled method. To reduce the mesh sensitivity around the crack tip , a non-local method is also applied to capture the spatial average value of the strain field within the potentially damaged area around the crack tips [22]. This locally-coupled method has been previously applied and demonstrated by [24] and [11, 33]. Figure 2.6 shows the crack model.

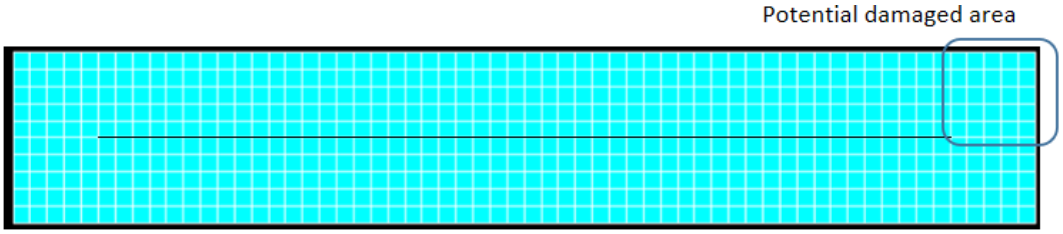

Figure 2.6: Crack model. The element size of crack model is 0.1mm. The crack length is 5mm, the potential damaged area is 0.5mm $\times$ 0.5mm

2.2.6. Meshing method

Both roller and raceway models are divided into three regions: contact area, transition area, and far field area, in accordance with the distance away from the contact area. The elements in the contact area should be fine enough to capture the precise stress/strain changes. In addition, crack area is also meshed in the contact area, see figure 2.7. The element size in the contact area is 0.2mm. As non- local method is used to capture the average value of the stress field or strain field in the potentially damaged area, the crack model is set up as shown in figure 2.6. In this model, the crack is simulated as a slit with two separate notch surfaces. The recommended element size in metals is $0.1mm^3$ in 3D [24], in our case this value is 0.1mm. Furthermore, due to the crack singularity, the element size of 0.05mm for crack model can cause numerical error i.e high distortion of the element around crack tip, resulting in non- convergence of strain value. Far-field area does not have much information about local issue. To reduce the computation time, the element size in far field area is as large as possible, i.e. 10mm. Meanwhile, high distortion of elements due to low quality of elements should be avoided. Furthermore, between the far field area and contact area, the elements sizes are different and the value of element size in transition area changes from small element size (0.2mm) to large element size (10mm). This scale factor of the transition area is 1.0653, which is calculated by a separate Matlab code.

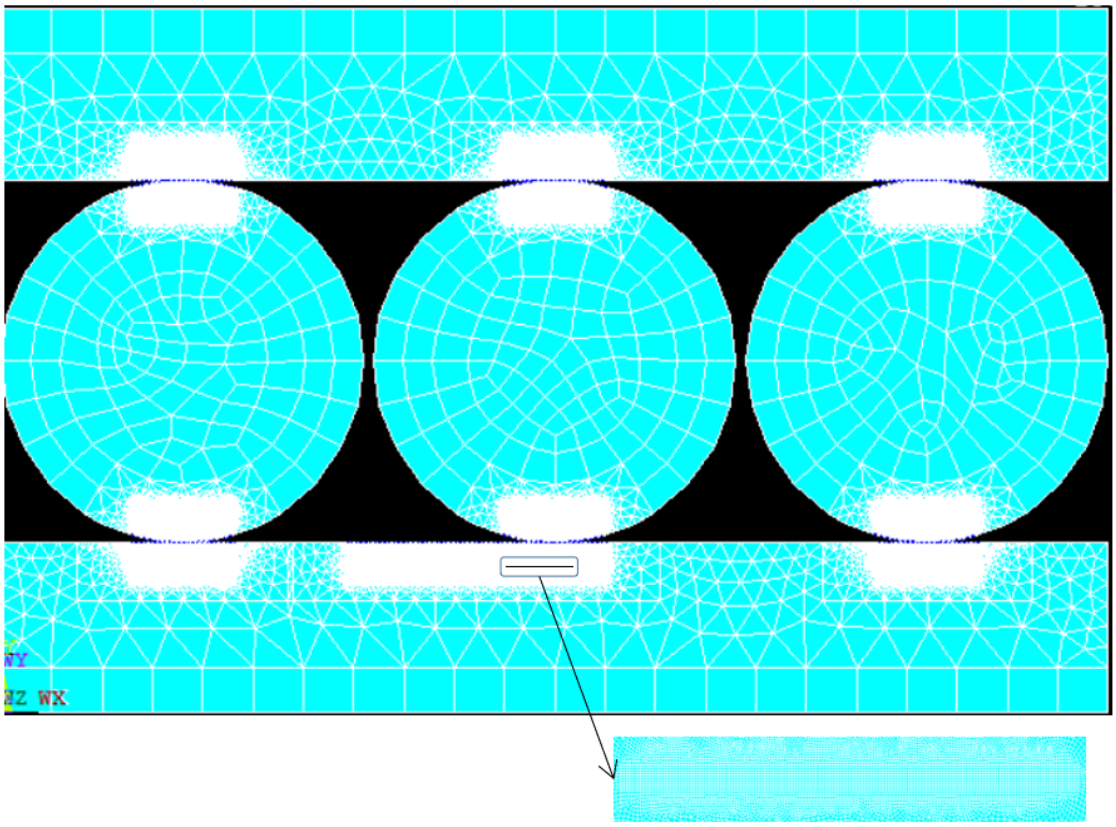

Figure 2.7: Global model. The black line is the crack model, the black block contains the area close to crack model.

2.3. Fatigue analysis

2.3.1. Fatigue model choice

For the purpose of investigating the remaining fatigue life of the defected roller bearing, the first step is to determine the fatigue regime type-low cycle fatigue or high cycle fatigue. Normally, low cycle fatigue is strain-based while high cycle fatigue is stress-controlled. When considering the fatigue model choice, three main inputs should be discussed: loading, material, and geometry model.

As discussed in the introduction, the low-speed roller bearing normally takes heavy loading, which is assumed high enough to initiate localisation of plasticity and thus cause the reduction in the stiffness of the material. In table 2.3, low load condition (at 163 KN) causes the elastic strain dominant which

means the high cycle fatigue regime should be taken into consideration. Since the high load condition (at least 1500 KN) is applied in this thesis, the plasticity strain is around ten times the elasticity strain, hence the plasticity should be considered into the fatigue analysis.

Furthermore, since the constant-amplitude strain loading is considered into the fatigue analysis, the Lemaitre's nonlinear damage law will be applied. In low cycle fatigue with constant amplitude strain loading, the elasto-plastic process can be stabilized after a few cycles. According to the linear Hooke's law, the reduction of material elastic modulus can reduce the nominal stress. From this respect, damage of the material can be expressed as the stiffness reduction, which can be indirectly measured by elastic modulus [24].

Table 2.3: Extreme values of plastic strain and elastic strain around the right crack front in the simulation. The crack length is 10 mm, and the crack front is located at the center of contact length (h=0, more details see figure 2.2, the loading conditions are separately 163 KN and 1500 KN)

Load cases	Strain values		
163 KN	ε^e_{xx}	ε^e_{yy}	ε^e_{xy}
	-0.20E-002	0.30E-002	-0.28E-002
	ε^p_{xx}	ε^p_{yy}	ε^p_{xy}
	0.33E-004	-0.11E-003	-0.34E-003
1500 KN	ε^e_{xx}	ε^e_{yy}	ε^e_{xy}
	0.40E-002	-0.51E-002	0.62E-002
	ε^p_{xx}	ε^p_{yy}	ε^p_{xy}
	0.14E-001	-0.23E-001	0.76E-001

Rolling contact fatigue generally takes place in the roller bearings. Moreover, the subsurface loading history in roller bearing is non-proportional, which causes the stress-strain response varying asynchronously with time in different directions. As illustrated in figure 2.8, when σ_{xx} is maximum at a certain time point, it does not mean that other stresses are also maximum at the same time. From this aspect, there is no unified standards in directions (xx, yy, xy) to determine fatigue failure. Considering the plasticity into fatigue, the energy release rate based on elastic strain is also considered. For energy release rate state for multiaxial fatigue, the equivalent stress criterion is normally the first choice [24].

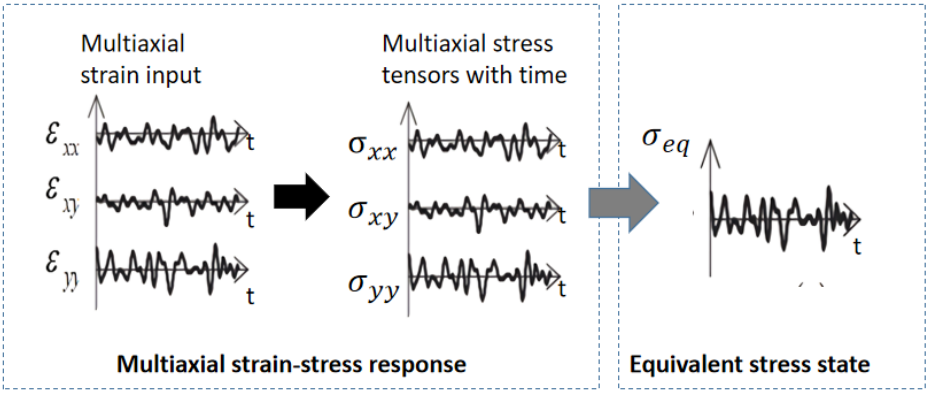

Figure 2.8: Multiaxial fatigue criterion transferring to equivalent criterion [34].

As illustrated in the figure 2.9, since the loading cycle is constant amplitude and non-proportional in low cycle regime, following the flowchart of the fatigue model choice, the last consideration is strain-life method or energy based method. Since the stress or strain alone is not sufficient to characterize the fatigue properties, energy-based model are applied, which combines the effects of stress and strain into released or dissipated energy during a load cycle [28].

As spalling is localised, and the damaged area due to spalling is small, compared with the whole scale of the roller-raceway model, the locally-coupled analysis is applied. This method is commonly

applied into metallic material due to homogeneous material character. For material such as concrete, this method is not applicable because the material is not homogeneous.

Locally-coupled method is more accurate than uncoupled analysis and has less computational time than fully-coupled analysis [24]. This method allows us to perform an uncoupled analysis at the meso scale of the whole structure, and then consider the coupling between strain and damage of the respective area to finish the post-processing damage growth. In this approach, the damage evolution is based on the energy release rate, so it means the damage accumulation is nonlinear throughout the entire loading cycles. In this research, however we only simulate one cycle of the roller passing. This means that, the results of strain history were in stable stage, ignoring the stress-strain response at the unstable stage (at the first few cycles).

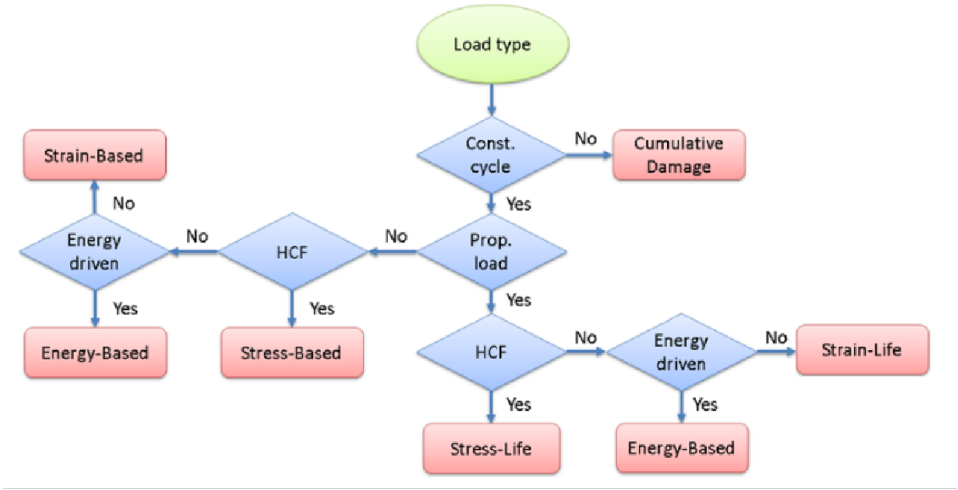

Figure 2.9: Fatigue model choice [28].

Damage evolution in the current damage state now is defined by the geometry model. The current damage is considered as the ratio between the crack length and the total raceway length. Figure 2.10 shows the final pattern of spalling is on the surface obtained experimentally. Figure 2.11 illustrates that the damage state in this research is bigger than the real state since the definition at our case ignores the transverse growth of spalling, as a result, the life estimation based on this damage state is under estimated. Meanwhile, for damage evolution, when damage reaches the last stage, the time for failure is very short which can be ignored.

In order to avoid singularity calculation issue on condition that $D = 1$, the damage threshold in this research should be set smaller than 1. In this case, this value is set as 0.7. The reason why larger values have not been chosen is that when the damage threshold is bigger than 0.7, the total damage accumulation at some crack sizes can be over 1 ($D > 1$) which is not physical. Meanwhile, the difference of lifetime obtained on the basis of threshold between 0.7 and larger value is tiny.

Figure 2.10: Final Spalling on the raceway surface[9]

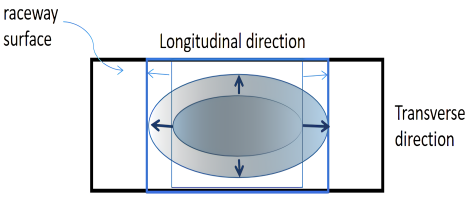

Figure 2.11: The spalling simplification [9]

2.4. Lifetime estimation

As locally-coupled method is considered, the nonlinear damage life estimation which is based on the energy release rate is applied in this thesis.

In life estimation, the energy release rate is mainly related to the equivalent stress and equivalent plastic strain. To get the failure number of cycles, the first thing is to get the integral of plastic strain in one circle. As damage increment is proportional to plastic increment, this integral is shown:

$$\frac{dD}{dN} = \int_{\text{cycle}} \dot{D}dt = \frac{\left(\frac{\Delta\sigma}{2}\right)^2}{2ES(1-D)^2} 2\int_0^t \dot{p}dt \tag{2.3}$$

Where: $\Delta\sigma$ is the equivalent stress range in one cycle.

In this research, since rolling contact fatigue produced the non-proportional loading history, the relationship between damage and plasticity is not simple. In practise, as crack grows, the amplitude of strain field at the crack tip is also variable, furthermore, the mean value also varies with the crack growth. In multiaxial fatigue especially non-proportional loading, the phase difference also varies, which enhance the difficulty of the estimation. These phase shifts are not easily to estimate by simple math equation. Furthermore, the energy based method are also sensitive to the loading history.

For simplicity, in fatigue, the damage is considered constant in one cycle. The damage increment in one cycle now is rewritten as follows:

$$\frac{\mathrm{d}D}{\mathrm{d}N} = \frac{(\sigma^*_{\max})^2}{2ES(1-D)^2}\Delta p \tag{2.4}$$

Where: Δp is the equivalent plastic strain amplitude range in one cycle. $\sigma^*_{\max}$ is the maximum damage equivalent stress [17], which is defined as the function of stress triaxiality and Von Mises stress.

$$\sigma^*_{\max} = max(\sigma_{\text{eq}} R_v^{1/2}) \tag{2.5}$$

The stress triaxiality R_v is shown as follows:

$$R_v = \frac{2(1+v)}{3} + 3(1-2v)\left(\frac{\sigma_{\text{m}}}{\sigma_{\text{eq}}}\right)^2 \tag{2.6}$$

When damage reaches the critical value, the failure is obtained and the obtained life cycle is registered. As for damage grows, more energy is released by breaking of the bonds. The energy release rate with damage is written as follows [24]:

$$Y = \frac{W^e}{(1-D)} = \frac{(\sigma^*_{\max})^2}{2ES(1-D)^2} \tag{2.7}$$

Where: W^e is the elastic strain energy density.

The life estimation is performed as a post-processing step after FEM. The principal strain does not directly show the variation of normal stresses and shear stress as damage accumulates from the definition of the effective stress[24]. Therefore, the principal strain is not considered firstly in this research. The flowchart of the life estimation is illustrated in the figure 2.12. The following is the steps for fatigue life estimation:

1. The input of the fatigue analysis is the spatial average values of strain data at xx, yy and xy directions. Then, the related vectors are transformed into the deviatoric state. The yield surface is firstly assumed as 0. The centre of the yield surface is initially assumed as 0. The initial damage is defined as the ratio of the length of the crack to the length of the raceway plate in the numerical model. The non-linear kinematic hardening rule (Ramberg-Osgood) is replaced by the linear segments, which means the radii of yield surfaces are known.

2. If the yield function is smaller than 0, the strain in xx, xy, yy is in the elastic regime, plastic strain is 0. If the yield function in Von Mises criterion is larger than 0, the plasticity corrector should be considered, which means i>0, until the yield function is smaller than 0. The equivalent Von Mises stress and equivalent plastic strain are obtained. In compression fatigue, considering the Lin-Taylor hypothesis and the principle of strain equivalence, the scale factor 0.28 is introduced and multiplied with $\mathrm{D_n}$ as the new $\mathrm{D_n}$, the derivative stress is rewritten as the equation 2.8 ([24], [15]) [1].

$$S_{ij} = \left((1 - 0.28\mathrm{D_n}) \times \mathrm{C_{ijkl}} \times \varepsilon\right)_{\text{dev}} \tag{2.8}$$

[1]The details of derivation process of damage accumulation in compression fatigue are discussed in [24].

3. Once the loading step is at the end of one loading cycle, the damage should be updated by applying the equation between maximum damage equivalent stress and equivalent plastic strain amplitude .
4. If damage is equal or larger than damage threshold, this loop is ended or repeat step 2-3.

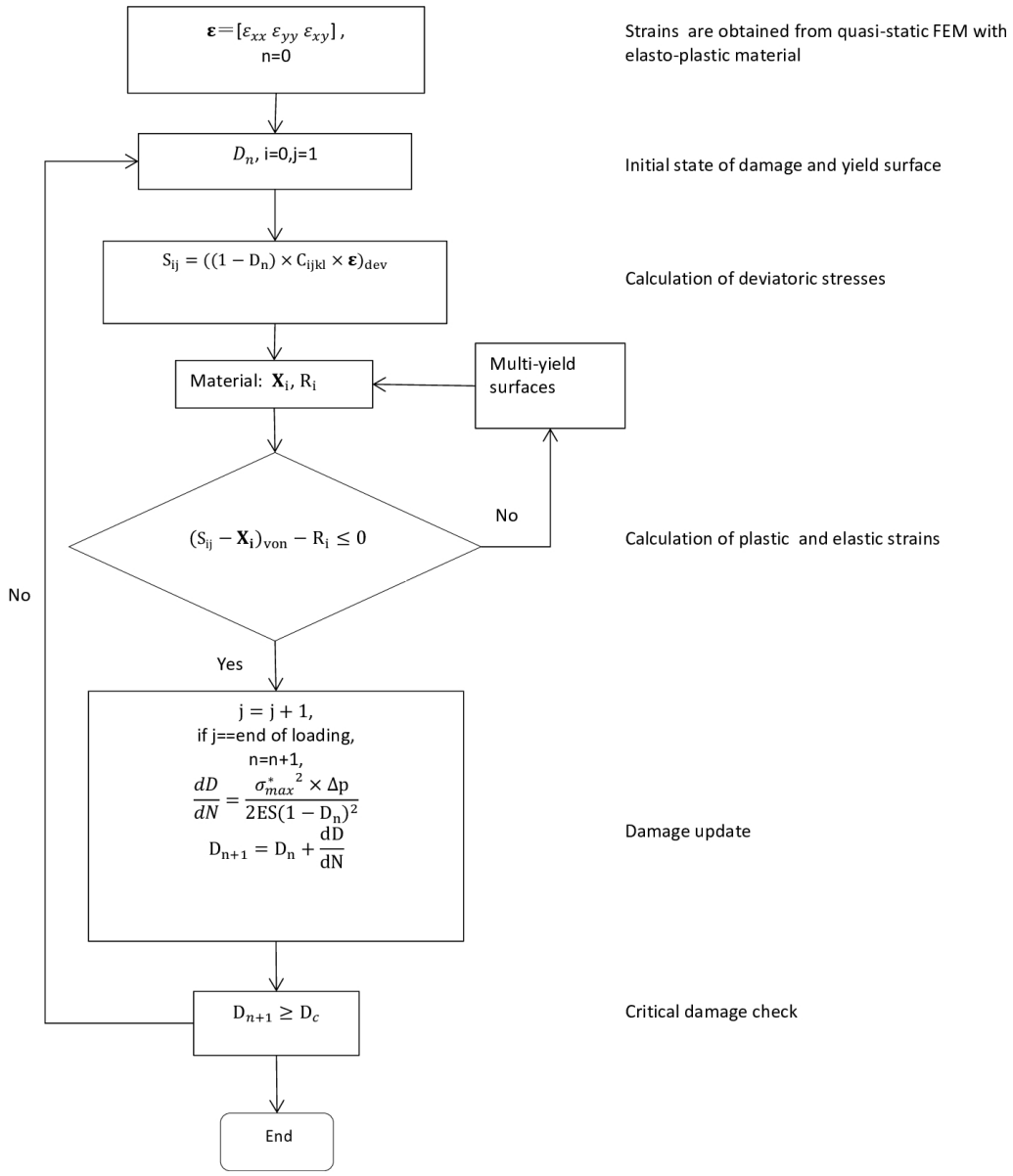

Figure 2.12: Flow chart of the life estimation

3

Results and discussions

3.1. Stress/strain field obtained from FEM

3.1.1. Convergence study

Coarse loading sub-step influence the convergence while fine sub-step sizes can increase the computation time. Therefore, the sub loading step size should be optimised. Element sizes near contact area are discussed in the following part.

The element quality is checked in the FEA model. The aspect ratio is evaluated of the elements, which can influence the distortion potential when highly-loaded case is experienced. For plane183 (which has mid-node element type), Jacobian Ratio normally helps to measure how the deviation of a given element is from an ideally shaped element. In this research, the quality of FEM is considered acceptable due to no element quality errors.

Observed from table 3.1, it can be found that: as element size becomes finer, the numerical results approaches to the Hertz theory results. Smaller element size means more elements and longer computation time. For element size is 0.5mm, the difference in the ratio of contact pressure is small while for the contact length, the difference ratio is large compared with other two element sizes. For the element size of 0.1mm, both contact pressure and contact length are closest to the Hertz theory at the expense of high element number.

Table 3.1: Comparison of Hertz theory and numerical solution of different element sizes in elastic material. The value in bracket show the difference ratio between numerical results and Hertz theory at 1510KN.

Element size (mm)	Element number [-]	Hertz Results		Numerical Results	
		Contact pressure (MPa)	Contact length (mm)	Contact pressure (MPa)	Contact length (mm)
0.1	92328			2647(1.3%)	3.54(6%)
0.2	26176	2612.3	3.32	2631(0.7%)	3.96(19%)
0.5	6126			2584(1%)	4.56(37%)

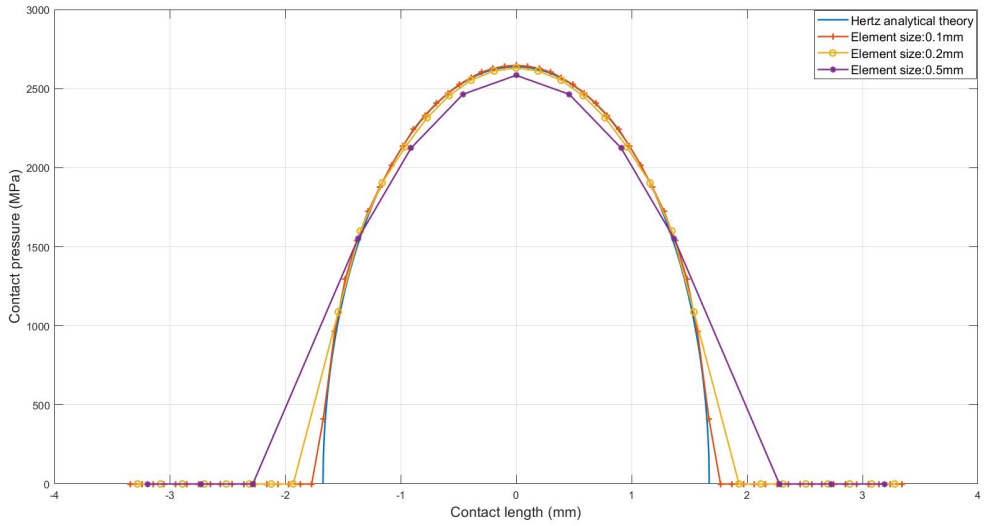

Figure 3.1: Comparison of contact pressure distribution in elastic material with different element size

When comparing the contact pressure in elastoplastic material at element size 0.1mm-0.2mm, the contact peak values are similar, but the element size at 0.2mm shows bigger contact length.

Compared with the element count for element size at 0.1mm, the element count at 0.2mm is small. Considering the accuracy and efficiency of computation, the element size at 0.2mm is our choice.

3.1.2. Contact pressure distribution in intact model

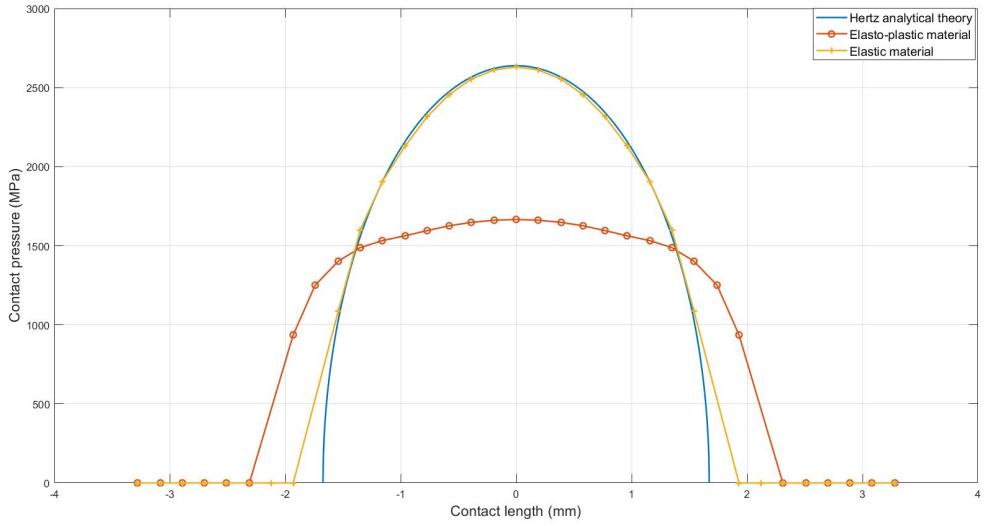

Figure 3.2: Comparison of contact pressure distribution in elastic material and elastoplastic material numerical results with Hertz theory results.

Hertz theory is proven as an accurate calculation of contact pressure and contact length in elastic material. As for elastoplastic material, due to the complication of plasticity, there is no accurate analytical method to calculate the contact pressure. This part will provide the qualitative analysis and comparison between the analytical solution and numerical solution in elastoplastic material. Figure 3.2 shows the comparison between numerical results and Hertz theory results. In elastoplastic material, the contact pressure is sharply reduced from 2631MPa to 1666MPa and the contact length is longer,

which is varied from 3.96mm to 4.62mm. These results are read from the middle roller. This is because with the existence of plasticity, the conformity of both roller and raceway is increased, which reduce the the height of contact surface. The results between elastic material and plastic material is shown in another example to be around 25% [14], while in our simulation the difference is 37%. Since the results of elastic material is in good agreement with Hertz theory, the element choice is considered acceptable. Note that: the loading condition in the example [14] is only around 10% of our setting up loading case and the steel yield strength is almost half of our cases . Furthermore, the friction parameter [14] is also considered as 0.35 while in our case it is assumed neglected. Considering the two FE models in different geometry and material parameters and the reasonable agreement with Hertz results, the plastic results of our model are regarded acceptable.

3.1.3. Contact pressure distribution for different crack front locations

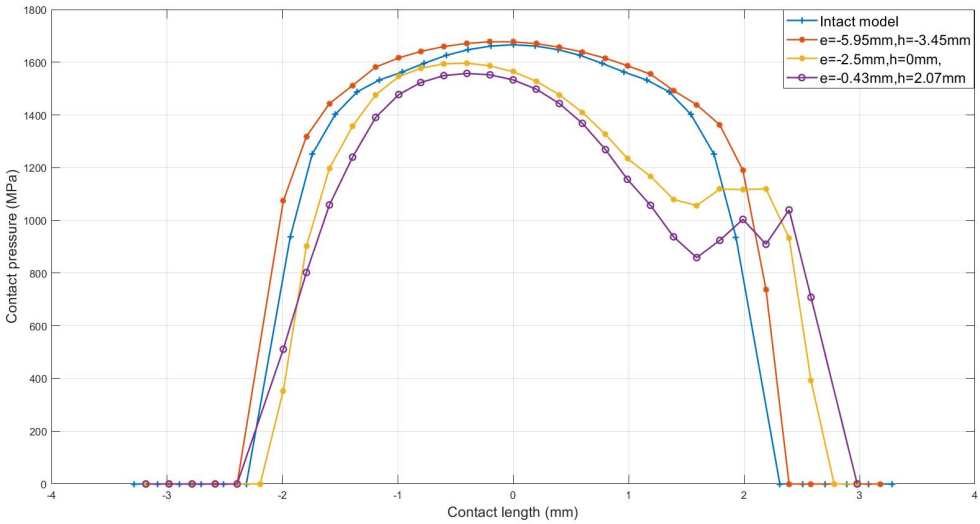

Figure 3.3: Comparison of contact pressure distribution of middle part of roller-raceway in different locations of crack front in elastoplastic intact and damaged models, where the crack length of damage models are 5mm, crack depth is 5mm. Here for e in the legend is referred in figure 2.2

In a damaged roller-raceway, the contact pressure distribution is different. As shown in figure 3.3, with the existence of crack with length of 5mm and depth of 5mm, the contact pressure between the raceway and the middle roller is subjected to lower value. Due to the existence of cracks, the local stiffness of the part of the raceway containing the cracks is decreased, resulting in a greater sinking for roller in the vertical direction. This sinking is slightly larger than that of the adjacent intact rollers. Therefore, the bearing capacity of the defective part is weakened. Meanwhile the adjacent roller and raceway without cracks have to carry more loads, which in return intensifies the uneven distribution of contact pressure among the rollers, and then prompts other parts to be prone to cracks more quickly. In other words, the existence of crack can reduce the contact pressure of the damaged part of roller and raceway, meanwhile the other two rollers have to resist more loads. When the crack tip is at 3.45mm, the whole crack is located outside of the half contact area (2.31mm). The crack existence slightly increases both contact pressure and contact length, with similar contact distribution with the intact model. From this respect, if crack is situated outside of the contact area, the influence of crack is more or less limited on the contact pressure distribution and contact length. When the crack is located within the contact area, the influence of crack is huge. The contact distribution has changed, and the peak value has also decreased and shifted along the direction with the crack length increase. This is possible because as the crack tip shifts from left to right, and the crack becomes more presented in the contact area, decreasing the stiffness of the cracked part, and subsequently the contact pressure is reduced. In summary, crack tip locations have influence on the contact pressure distributions and peak values. The influence range is dependent on whether the crack is outside or inside of the contact area.

Table 3.2: Peak value of contact pressure at the free surface of raceway

	Intact model	$h = -3.45$mm	$h = 0$mm	$h = 2.07$mm
Left roller-raceway(MPa)	1661	1689	1689	1689
Middle roller-raceway (MPa)	1666	1671	1596	1552
Right roller-raceway (MPa)	1662	1689	1689	1689

As illustrated from table 3.2, the contact pressure are almost same for all three rollers in the intact model. On the other hand, the presence of crack influences the cracked roller-raceway largely. For the neighbouring rollers, the influence is limited since the crack in this model is more like a local issue, and the influence also remains mostly local.

3.1.4. Contact pressure distribution for different crack lengths

In this subsection, the impact of the initial crack length is discussed. To make sure the crack length is the only variable, the length of crack part under the contact area is constant and equals to half the contact area length (2.31mm). The loading condition is the same.

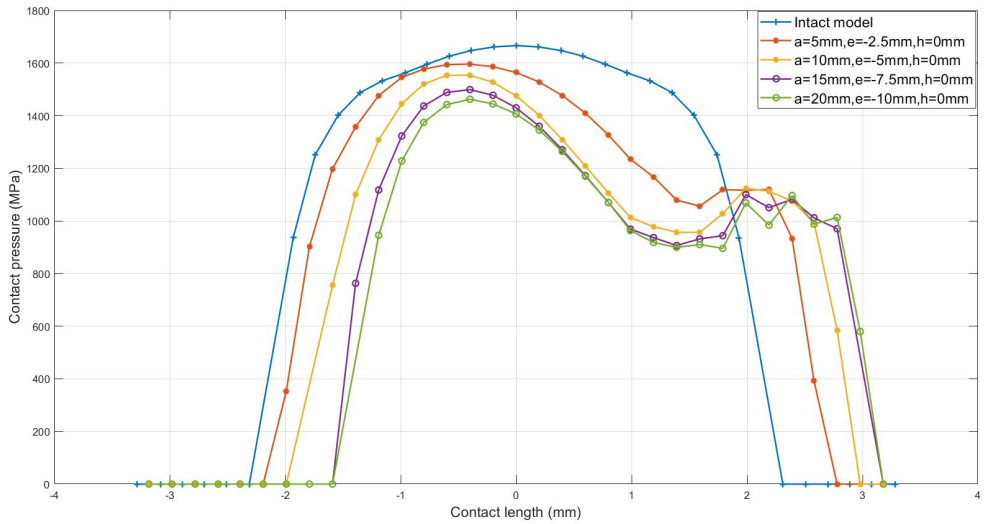

Figure 3.4: Comparison of contact pressure distribution in different crack lengths at same crack front location in elastoplastic intact and damaged models, where the crack length of damage models are 5 - 10 mm, crack depth is 5mm. Here for e in the legend is referred in figure 2.2.

The contact pressure distribution in different crack length is illustrated in figure 3.4. It is observed that the peak value of contact pressure is reduced compared with the intact model as the crack length increases. When it comes to the contact pressure distribution, it is more pronounced with the increase of crack length. Furthermore, the increase of crack length also makes the contact pressure distributions move to the right, and a second peak occurs at the edge of contact area. The range of contact pressure changes caused by increasing crack length decreases, especially in the arrange between 5mm - 10mm and 15mm - 20mm. In other words, the crack length has influence on the contact pressure distribution and for longer crack is , the contact pressure distribution seems to converge. Following this trend, when crack length grows to a critical value, the contact pressure distribution reaches at the ”constant” state. For the neighbouring contact pressure, the crack influence seems limited (as also explained in the former subsection), as illustrated in table 3.3. The reason why contact pressure distribution varies as such trend is that the crack grows between 5mm - 20mm at the unstable speed due to the remaining plasticity.

In summary, the contact pressure distribution is not only influenced by the plasticity but also the crack existence. In return, the contact pressure distribution also have impacts on the crack, which means the contact pressure and crack influence each other. Since the difference of contact pressure between

15mm-20mm, and 10mm-15mm is smaller than 5mm-10mm, in other words, the start of monitoring crack length bigger than 10mm is more meaningful than the start at or less than 5mm.

Table 3.3: Peak value of contact pressure at the free surface of raceway

	Intact model	$a = 5$mm	$a = 10$mm	$a = 15$mm	$a = 20$mm
Left roller-raceway(MPa)	1661	1689	1690	1685	1686
Middle roller-raceway (MPa)	1666	1596	1554	1499	1463
Right roller-raceway (MPa)	1662	1689	1689	1685	1686

3.1.5. Contact pressure distribution for different crack depths

As seen in figure 3.5, the only variable is the depth. For damaged model, the contact pressure distribution shifts to the right. However, the movement at the depth of 6mm is smaller than that at depth of 5mm. Furthermore, the peak value at the depth of 6mm is bigger than that at 5mm. Additionally, both peak value are smaller than intact model. In a word, as the crack depth increases, the influence of crack is smaller on the contact pressure. The specific of peak values are shown in table 3.4.

Table 3.4: Peak value of contact pressure at the free surface of raceway

	Intact model	$d = 5$mm	$d = 6$mm
Left roller-raceway(MPa)	1661	1690	1690
Middle roller-raceway (MPa)	1666	1554	1614
Right roller-raceway (MPa)	1662	1689	1690

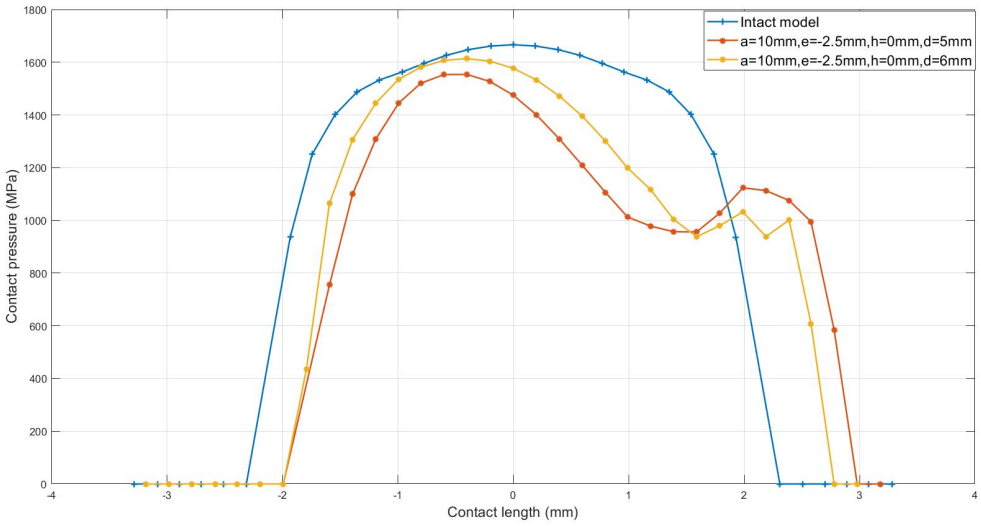

Figure 3.5: Comparison of contact pressure distribution in different crack depths at same crack front location in elastoplastic intact and damaged models, where the crack length of damage models is 10mm. Here for e in the legend is referred in figure 2.2.

3.1.6. Stress/strain field for damaged model

The former sections discussed how the contact pressure distribution varies due to crack. This section is focus on the variation of stress/ strain field around crack tip in the subsurface of the contact area.

When compared to the dynamic simulation, the complete stress/strain history of quasi-static simulation cannot be shown. To capture the stress and strain history as much as possible, there remain only 11 discrete locations along the contact length. Based on the 11 discrete locations, the main character of stress/strain field around crack tip within the contact area can be obtained. The following figures are the stress field around crack tip in 11 discrete locations for different crack lengths in comparison with the intact model at the same depth. The trend of σ_{xx} shown in the figure 3.6 is similar for the shown four crack lengths. As the crack length increases, the stress field becomes also larger. But the difference of stress increase is not proportional with the crack length increase. The 15mm and 20mm are more like 10mm translations in the vertical direction, and they are more or less centrosymmetric around point $(0, -300)$, while intact model results are symmetric at $x = 0$. However, the stress distribution at for the crack length of 5mm is different from other three crack lengths. Compared with the intact model, the location of maximum value shifts from center to the edge, while the minimum value is situated at the edge of contact area. As for the following fatigue estimation, the considered locations are assumed as one cycle. The difference of location of extreme values means the phase shift between cracked part and intact part. The reasons for this phase shift are complex, caused by the details of the geometry material properties and plasticity.

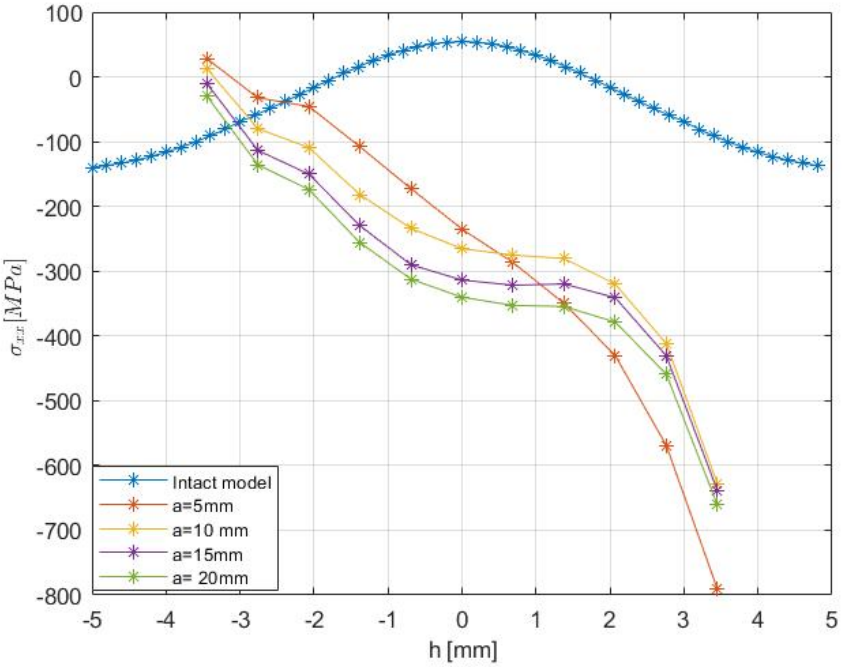

Figure 3.6: σ_{xx} at discrete locations under the contact area

The trend of σ_{xy} is similar for considered four crack lengths. But the stress raise does not vary in proportion with the crack length increase. In the intact model, the stress distribution is centrosymmetric around point $(0, 0)$. As for the cracked model between 10mm and 20mm, the trend of shear stress distribution is similar to the intact model. However, the extreme value locations are marginally changed. The results for crack length of 5mm is different from other three cracked cases. The maximum value at 5mm is also larger than the intact model and the distribution is not centrosymmetric. The phase shift of shear stress occurs within the range from intact to small crack length such as 5 mm.

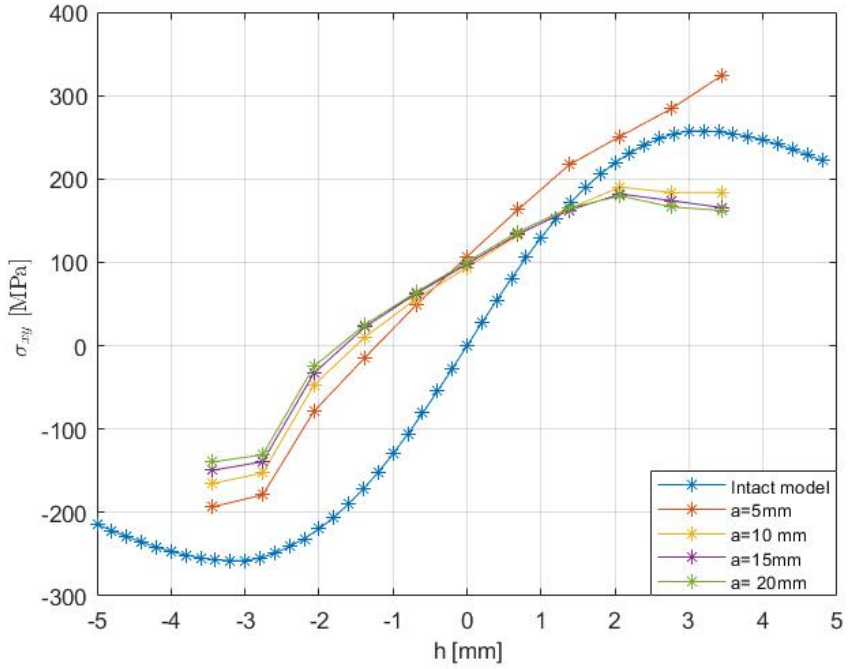

Figure 3.7: σ_{xy} at discrete locations under contact area

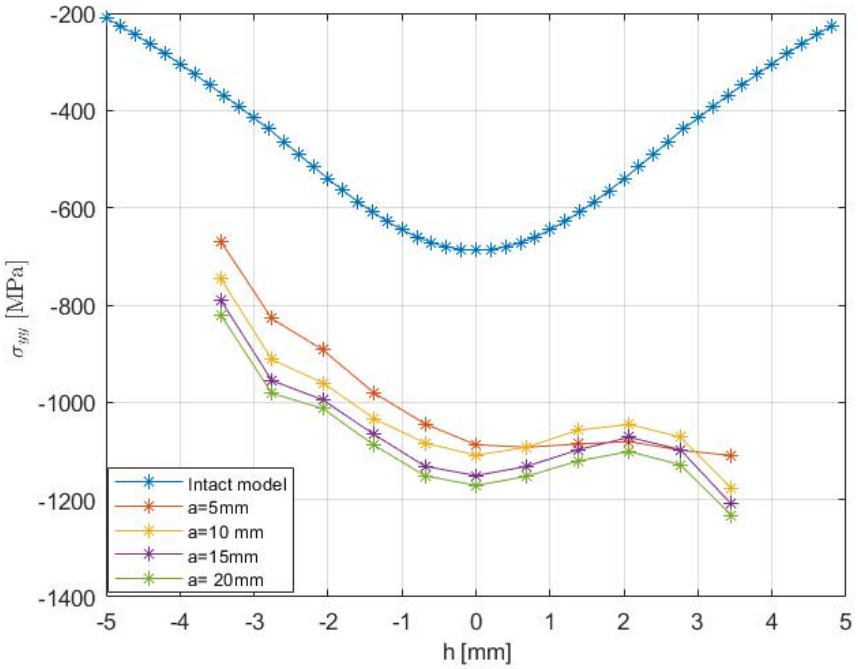

Figure 3.8: σ_{yy} at discrete locations under contact area

The general trend of σ_{yy} is comparable for the different crack length. All of the amplitude are negative. This is because the loading condition in yy direction is compression. For the crack length of 5mm, the trend of stress drop is slightly different from the other three crack sizes, possibly due to sharp local variations.

The following figures are about the strain field around the crack tip. Without a present crack, the strain field in different directions are around 0. However, due to the crack presence, the strain amplitude are enlarged and the mean strain also shifted away from 0. Compared with stress variation, distribution of ε_{yy}, ε_{xx}, ε_{xy} for different crack sizes are similar under contact area.

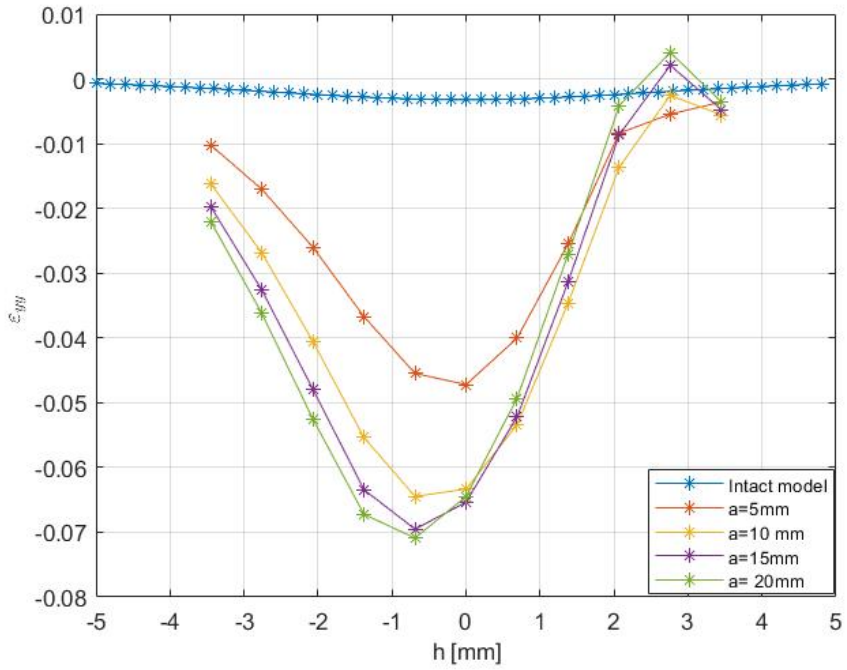

Figure 3.9: ε_{yy} at discrete locations under contact area

When it comes to ε_{yy}, the extreme values are negative. The maximum value at the intact model is 0.003. Due to the crack existence, the maximum value for crack length of 5mm are at least 16 times bigger than the intact case, while the enlarge scalar at 20mm case is 30. The interval among 10mm - 20mm is smaller than the difference between 5mm and 10mm. Like cases of stress field, the strain distributions for the crack length of 5mm are different from other three crack cases.

The strain distributions of yy and xx (shown in the figure 3.9 and figure 3.10) are almost symmetrical at $h = 0$. The values are mostly positive and the maximum value at the intact model is 0.0016, which is neglieible compared to the cracked cases. All extreme value at xx direction is smaller than that in yy direction.The maximum values shifted from $h = 0$ to left among cracked models.

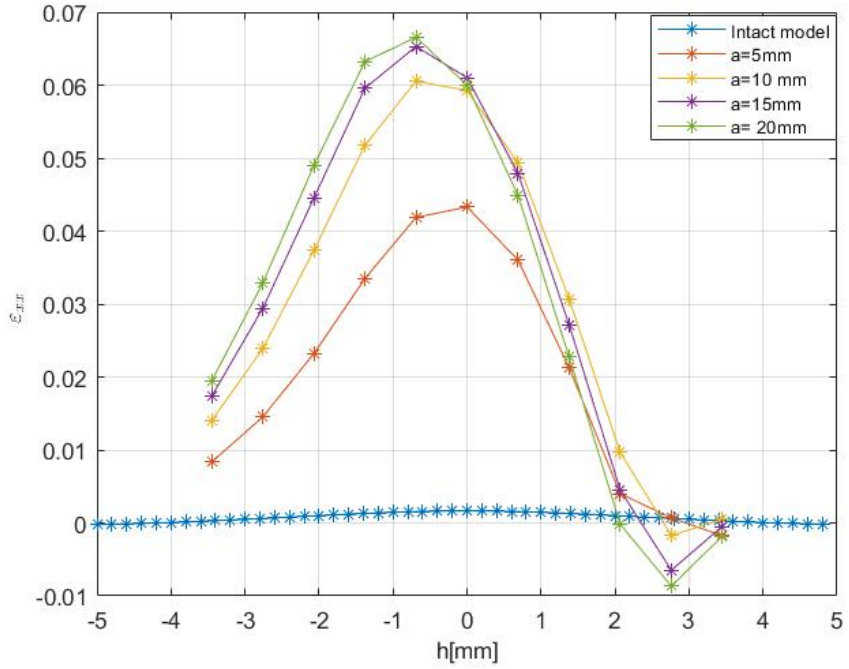

Figure 3.10: ε_{xx} at discrete locations under contact area

The shear strain is maximum for the crack length of 20mm close to 0.16. This is a relatively large value, but since $\varepsilon_{xy} = \varepsilon_{yx}$, the shear strain shown in the figure 3.11 is the twice of ε_{xy}. The phase shift only occurs between intact and cracked cases. From 5mm to 20mm, the extreme values lie at the same location. The maximum value at the intact model is 0.0017, which is considered very small.

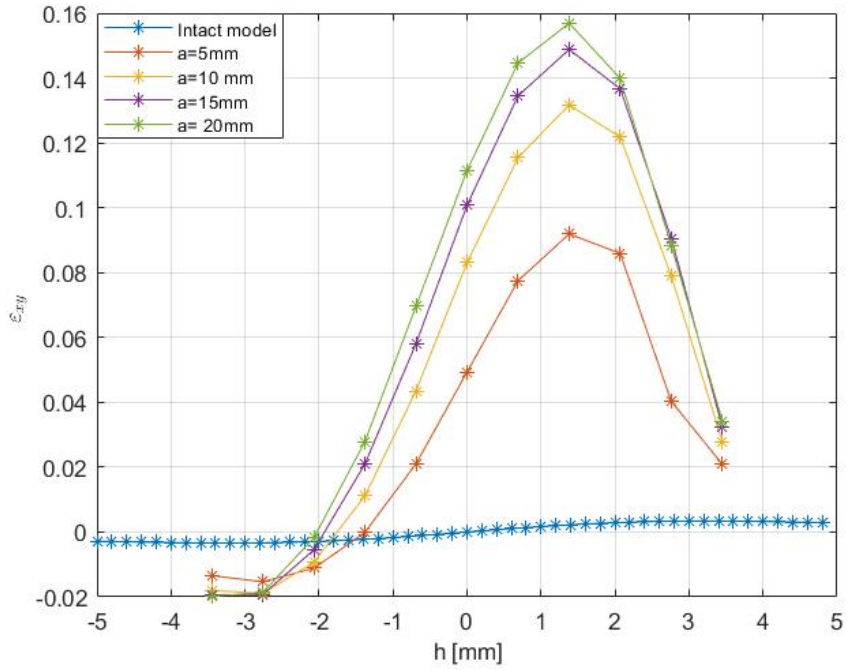

Figure 3.11: ε_{xy} at discrete locations under contact area

In summary, the stress field is not notably sensitive to the crack length contrary to the strain field.

This is because according to the stress-strain response, when plastic strain grows, the stress increases at steps. Considering the crack singularity and sensitivity for the variation of crack length, the loading input for damage calculation should be the strain field instead of the stress field. On the other hand, as the crack grows, the total strain is increased in different directions. Furthermore, shear strain at the small cracked model and intact model is not dominant, but in longer crack length model, shear strain becomes dominant.

3.2. Remaining life predictions

Cracks with branches can be simply viewed as changes in length and depth in 2D. Therefore, this section will analyze two conditions about different lengths and depths of cracks.

The results of the rate of damage accumulation are shown in the figure 3.12. The beginning of damage increment before 100 cycles remains constant among the crack range 10mm-20mm. However, when it comes to crack size as 5mm, this steady-state remains for 1000 cycles. Similar growths of damage increment are seen among the crack sizes from 5mm to 20mm. This figure also shows that there has been a sharp increase of damage increment for the crack size between 10mm -20mm after 1000 cycles. However, for the crack size of 5mm, this sharp increase has occurred after 2000 cycles. The threshold of damage increment for the crack size of 20mm has peaked close to 2.5×10^{-3}. Compared with other three damage increment thresholds, that for crack size as 5mm reached a lowest point, which is smaller than 1.5×10^{-3}. In summary, the damage accumulation of crack size as 5 mm is different from the other three crack sizes. This is because the strain input for crack size as 5mm is smaller than that for the other three crack sizes.

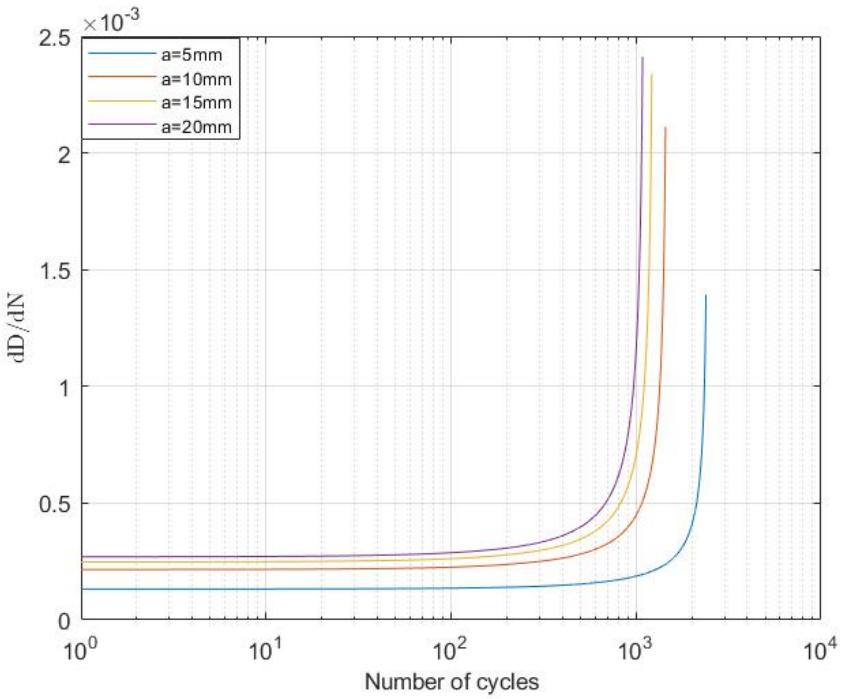

Figure 3.12: Rate of damage accumulation for different crack sizes at the same depth d =5mm.

As the rate of damage accumulation becomes larger, the damage rise up quickly. When the damage reached the threshold, the total life cycle are obtained. Figure 3.13 shows the process of damage evolution for different crack sizes. The initial damage value is set up differently for different crack sizes. The longer the crack size is, the larger the damage initial value becomes. According to the equation 2.4, as the rate of damage accumulation goes up, larger damage in return accelerate the damage accumulation. Furthermore, as seen in the figure 3.13, these four damage evolution lines are almost parallel. From right to left, the distance between two adjacent lines becomes smaller.

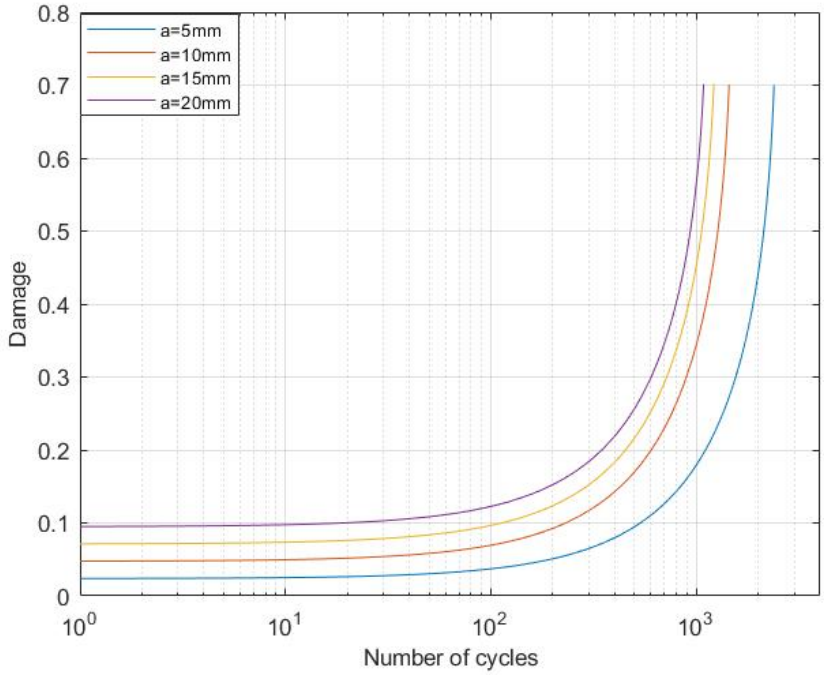

Figure 3.13: Damage evolution for different crack sizes at the same depth d=5mm.

As seen in the figure 3.14, all of the lines starts from zero. At the second cycle, the value of equivalent stress at the crack size as 5mm is around 850 MPa, while that at the crack size as 20mm is around 700 MPa. This is possibly caused by different initial damage values. As the damage threshold is 0.7, the last maximum damage equivalent stress can be around 255 MPa by the rough calculation 3.1. However, the last maximum damage equivalent stresses between 10mm and 20mm are less than 200 MPa. This is possible because the decrease of stress is not only related with the damage but also the stress at the previous one cycle instead of initial stress. At the beginning, plastic strain is constant, which means the elastic strain is also stable at constant strain loading. As damage evolution, plasticity is decreased, then the elasticity is increased, but due to the elastic modulus is decreased and back stress evolved, the equivalent damage stress drops down. From this aspect, the equivalent damage stress decrease is nonlinear. Furthermore, the difference between initial state and last state decreases as crack increases from 10mm to 20mm. One of the reasons is that the damage accumulation is different, which is illustrated in the figure 3.12.

$$\sigma_{max}^{last} = (1 - 0.7)\sigma_{max}^{initial} \tag{3.1}$$

Other three crack sizes go down as similar trend while crack size at 5mm goes down with smaller steps. Furthermore, the equivalent stress at the end of the life cycle is largest for the crack size as 5mm. At 120^{th} cycle and among $500^{th} - 1100^{th}$ cycle, there remains small fluctuating points for crack size as 5mm, which is caused by instability of the explicit algorithm. This small fluctuating point is also seen at the cycle range of $100^{th} - 300^{th}$ for crack sizes between 10mm and 15mm. The turning point of dropping rate appears between 350^{th} and 550^{th} for crack size between 10mm and 20mm in the figure 3.14 due to the decrease in plasticity.

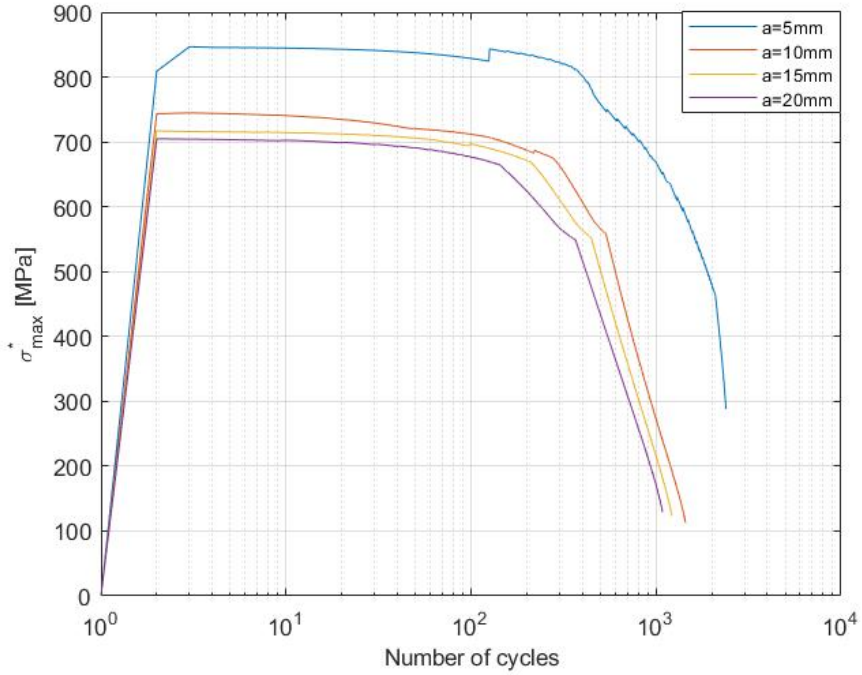

Figure 3.14: Equivalent stress with the cycles for different crack sizes at the same depth d=5mm

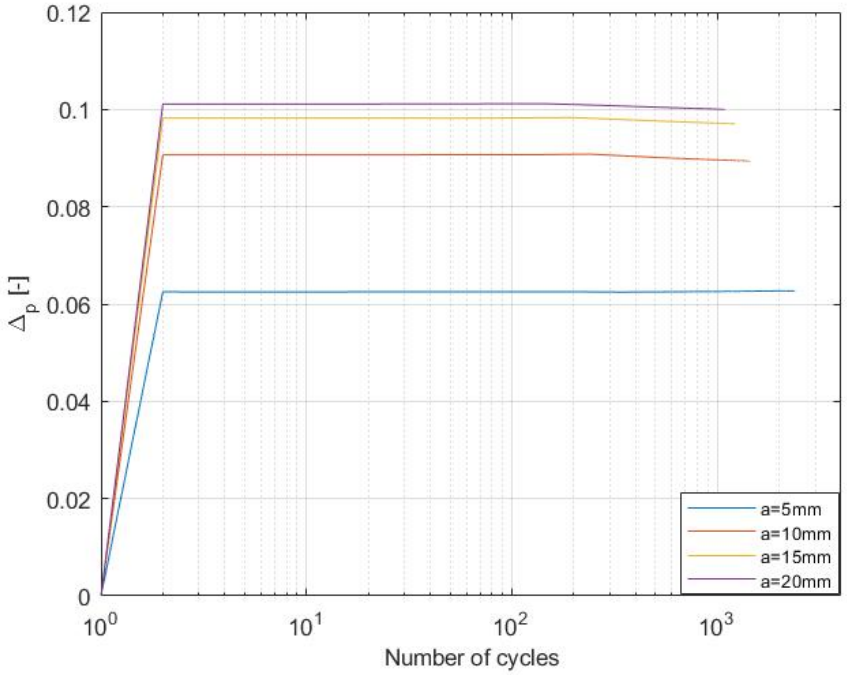

Figure 3.15: Equivalent plastic strain amplitude with cycles for different crack sizes at the same depth d=5mm

It is seen in the figure 3.15, the plastic strain amplitude for 5mm is much smaller than the other three results, and the plastic strain amplitude between 15mm and 20mm is close. All of the plastic strain amplitude is almost constant. This is because the loading condition in the fatigue estimation is constant amplitude, but due to the instability of the algorithm, this constant amplitude decreases with a small range. Another reason may be that metal at different hardness levels have different hardening or softening behaviors. This means if we want to get more accurate life estimation, the material hardness character should be obtained accurately.

The damage growth, plastic strain amplitude, equivalent stress variation between 15mm and 20mm are similar. From this aspect, the maximum horizontal crack size may be between these two values. Considering the low cycle fatigue and FEM results, crack size of 5mm has a different trend with others while that of 10mm has a similar trend with 15mm and 20mm, so the minimum detectable crack size of 10mm is more meaningful than that of 5mm.

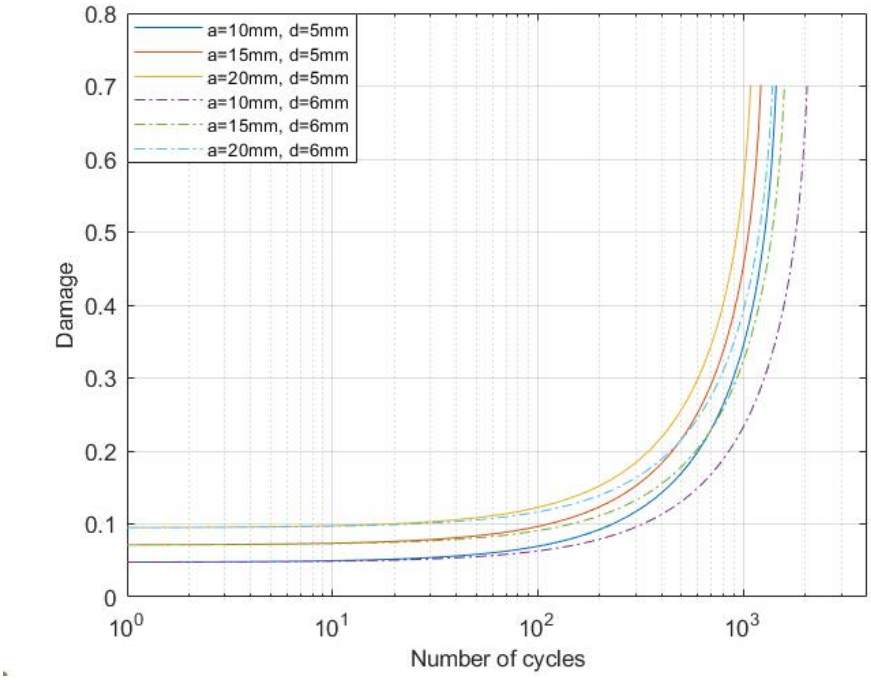

Figure 3.16: Damage evolution with cycles for different crack sizes at different depths

As illustrated in figure 3.16, the distance between two adjacent groups of life cycles at a depth of 6mm is larger than that at a depth of 5mm. The life cycle based on the crack size as 20mm at depth of 6mm is almost equal to that of crack size as 10mm at depth of 5mm. However, the life cycle of crack size as 10mm at depth of 6mm is close to that of the crack size as 5mm at depth of 5mm.

As shown in figure 3.17, the initial stresses at depth of 6mm are all smaller than those at depth of 5mm. The minimal stresses are smaller than 200MPa. As seen in figure 3.18, the plastic strain amplitudes at the depth of 6mm are also smaller than those at the depth of 5mm.

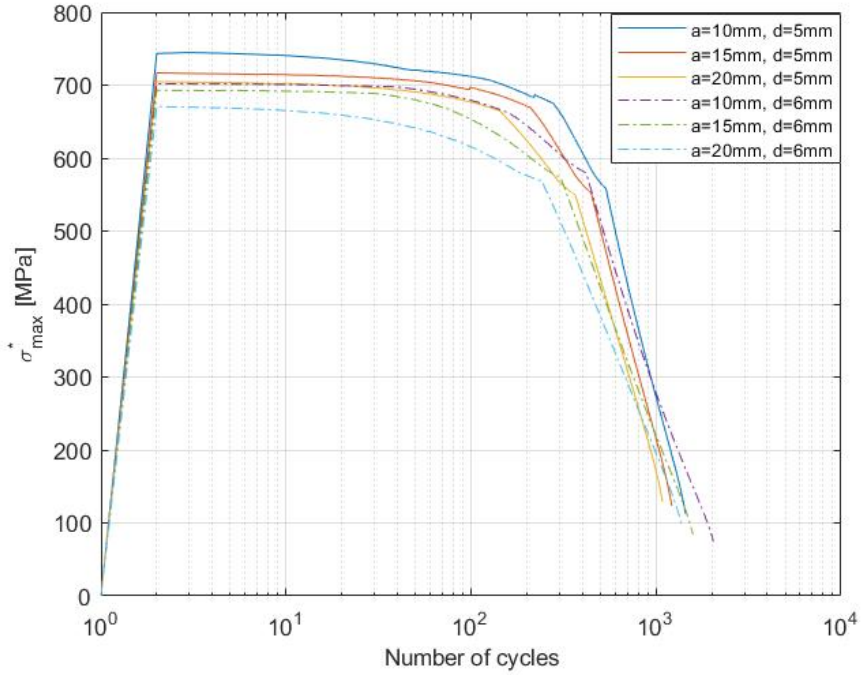

Figure 3.17: Maximum damage equivalent stress with the cycles for different crack sizes at different depths.

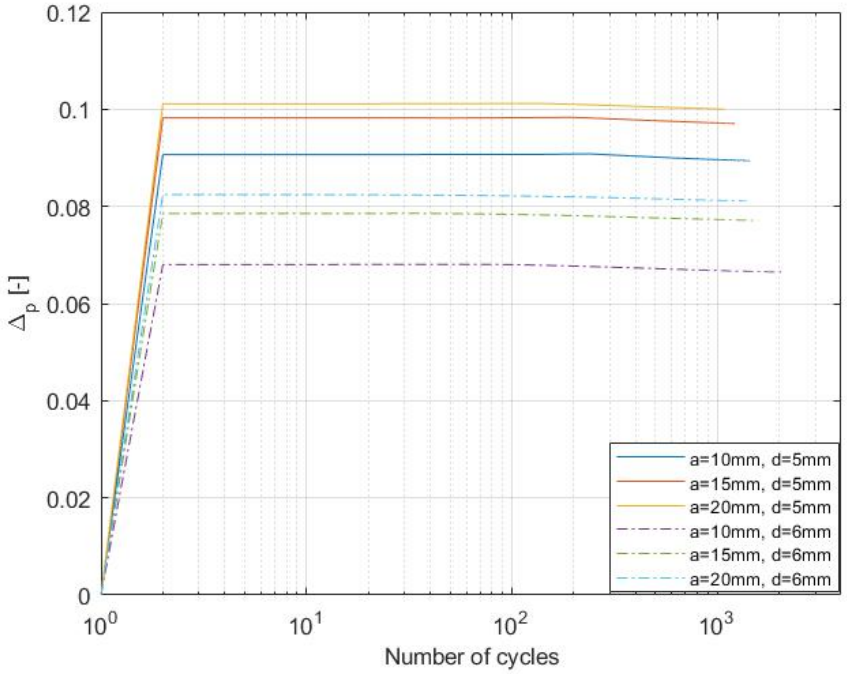

Figure 3.18: Equivalent plastic strain amplitude with the cycles for different crack sizes at different depths.

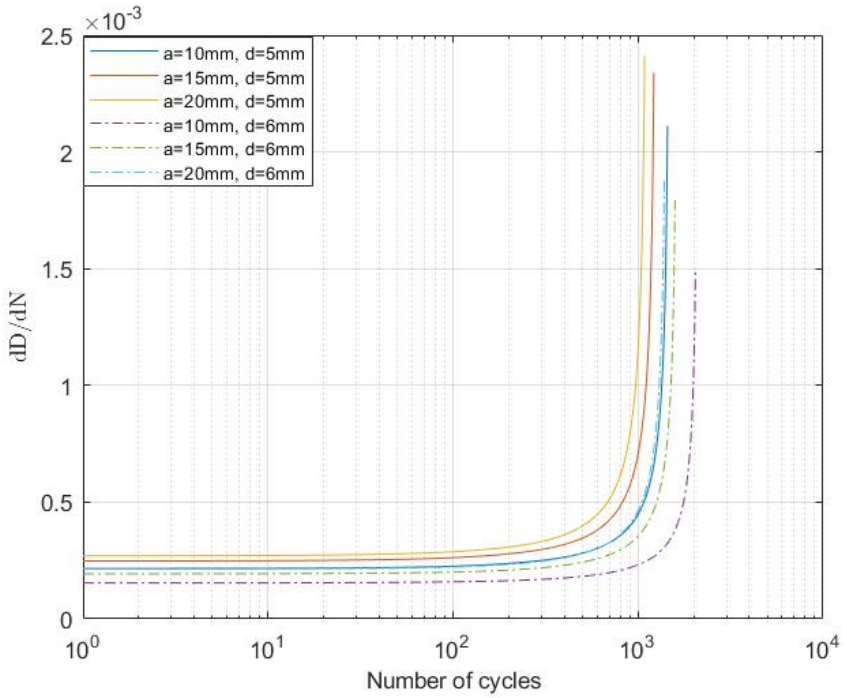

Figure 3.19: Rate of damage accumulations with cycles for different crack sizes for different depths

As seen in figure 3.19, the damage increment at the depth of 6mm has accumulated slower than that at the depth of 5mm. The threshold of damage increment for the crack size of 20mm at depth of 6mm has peaked close to 1.8×10^{-3} while this value has reached 2.4×10^{-3} at the depth of 5mm. The threshold of damage increment for crack size as 10mm at depth of 5mm reached close to 2.1×10^{-3}, meanwhile this value at depth of 6mm is 1.5×10^{-3}. At crack size of 20mm, the difference of threshold of damage increment between two depths is 0.6×10^{-3}. However, at the same depth of 5mm or 6mm, this difference between 10mm and 20mm is 0.3×10^{-3}, which has cut in half of former difference.

In a word, a 1mm depth increase can reduce the damage increment and enhance the remaining life cycles for damage evolution and this influence is higher than the influence of the decrease of 10mm in crack size. In other words, the influence of depth are larger than that of crack size.

4

Conclusion and recommendations

Feasibility of using monitoring information for prognosis of the remaining life of heavily-loaded low-speed bearings was investigated. A locally-coupled damage accumulation model based on Lemaitre damage growth was developed for subsurface raceway cracks, which takes the existing crack (notch) sizes and locations as input.

The proposed damage growth model can provide an initial estimate for the remaining life cycles of the damaged slow-speed roller bearings. Furthermore, the plasticity and Von Mises stress changes can be captured in this damage growth model. However, the quality of this estimation and possible improvements require further an experimental assessment.

Different from the direct influence of surface cracks on the contact pressure, the cracks under the surface also have an influence on the contact pressure, but this influence depends on whether the crack is within the contact area or not. Within the contact area, both crack size and depth can have a positive or negative impact on its contact pressure, although due to the localization, this impact is limited. Outside of the contact area, a crack has rarely influence on the remaining life estimation. The strain field data turned out to be more sensitive to these two damage parameters compared with the stress field. It is reasonable to apply the strain field data into the remaining life estimation. However the stress field data is not recommended to be applied as input for the remaining life estimation in this research.

The influence of two damage parameters i.e crack size and crack depth, are discussed in this research in the heavily-load condition. Both damage parameters have influence on the estimated remaining life cycles. Crack size is positively correlated with life prediction while crack depth is the opposite. Additionally, the influence of depth on the remaining life cycles estimation is larger than that of crack size.

In the range of the crack size between 10mm and 20mm, there remains similarity in stress and strain field. Shorter cracks may have different stress and strain field distribution.

Plasticity plays an important role in the remaining life estimation. In fact, it is found that the magnitude of plastic strain is relevant to the crack size and crack depth. As crack size becomes larger, plastic strain also becomes larger. However, plastic strain is negatively related to crack depth.

Minimum detectable damage size with the current monitoring technology is considered about 10mm. What's more, detection is needed before the crack grows towards 15mm-20mm. However the difference of the number of cycles to failure is small between the detectable crack size (10mm) and the critical crack size (15mm) at the same depth. Further improvement of the monitoring system for detection of smaller cracks is needed.

It is acknowledged that several conditions in this research were idealised. The influence of friction was not discussed in this research, which is different from the practice. To improve the estimation, it is recommended to consider the friction influence into the life estimation. The material is considered homogeneous, but in practise production, non-metallic inclusion can be presented. Non-metallic inclusions of different chemical compositions and the distance from the crack will have an impact on the remaining life analysis. For future research, this topic is also suggested to be considered.

The fully-coupled damage mechanism with constitutive models in FEM was not considered in this research. For future work, the extended finite element method (XFEM) coupled with the damage

mechanism is recommended to overcome the numerical challenges. Additionally, another method e.g phase-field method, may be considered to simulate crack in low cycle regime for future work.

Bibliography

[1] M. Ambati, T.Gerasimov, and De Lorenzis. Phase-field modeling of ductile fracture. *Computational Mechanics*, 55(5):1017–1040, 2015.

[2] MC. Araujo. Non-linear kinematic hardening model for multiaxial cyclic plasticity. *International Journal of Fatigue*, 30:1985–1996, 2002.

[3] A.Warhadpande, F.Sadeghi, M.Kotzalas, and G.Doll. Effects of plasticity on subsurface initiated spalling in rolling contact fatigue. *International Journal of Fatigue*, 36(1):80–95, 2012.

[4] J. Bomidi and F. Sadeghi. Three-dimensional finite element elastic–plastic model for subsurface initiated spalling in rolling contacts. *Journal of Tribology*, 136(1), 2014.

[5] MF Borges, DM Neto, and FV Antunes. Numerical simulation of fatigue crack growth based on accumulated plastic strain. *Theoretical and Applied Fracture Mechanics*, 108:102676, 2020.

[6] P.O. Bouchard, F. Bay, and Y. Chastel. Numerical modelling of crack propagation: automatic remeshing and comparison of different criteria. *Computer methods in applied mechanics and engineering*, 192(35-36):3887–3908, 2003.

[7] B.Scheeren, F.Riccioli, A.Huijer, N.Thakoerdajal, and L.Pahlavan. Hiteam phase 2 final technical report, 2021.

[8] Huisman Equipment B.V. Huisman equipment: Pipelay. `https://www.huismanequipment.com/afbeeldingen/products/pipelay/intro/_resized/pictures_-_flexlay-_website_w520_h320_bg.jpg`, 2013.

[9] B.Yazdizadeh. Comparison of different plane models in finite element software in structural mechanics. *Proceedings of the YSU, Physical and Mathematical Sciences*, pages 44–50, 2010.

[10] R. Desmorat. Damage and fatigue: continuum damage mechanics modeling for fatigue of materials and structures. *Revue européenne de génie civil*, 10(6-7):849–877, 2006.

[11] R Desmorat and J Lemaitre. Crack-initiation conditions: extended neuber method coupled to damage mechanics. *WIT Transactions on Engineering Sciences*, 19, 1998.

[12] S. Diel and O. Huber. A continuum damage mechanics model for the static and cyclic fatigue of cellular composites. *Materials*, 10(8):951, 2017.

[13] G. Donzella, A. Mazzù, and C.Petrogalli. Experimental and numerical investigation on shear propagation of subsurface cracks under rolling contact fatigue. *Procedia Engineering*, 109(1): 181–188, 2015.

[14] HM. El-sayed, M. Lotfy, HN El din. Zohny, and HS. Riad. Prediction of fatigue crack initiation life in railheads using finite element analysis. *Ain Shams Engineering Journal*, 9(4):2329–2342, 2018.

[15] F.Marina, B.Robert, and P.Ivan. Genetic algorithm in material model parameters' identification for low-cycle fatigue. *Computational Materials Science*, 45(2):505–510, 2009.

[16] F.Sadeghi, B.Jalalahmadi, T. Slack, N. Raje, and N. Arakere. A review of rolling contact fatigue. *Journal of tribology*, 131(4), 2009.

[17] F.Shen and K.Zhou. An elasto-plastic-damage model for initiation and propagation of spalling in rolling bearings. *International Journal of Mechanical Sciences*, 161:105058, 2019.

[18] Y. S. Garud. A New Approach to the Evaluation of Fatigue Under Multiaxial Loadings. *Journal of Engineering Materials and Technology*, 103(2):118–125, 04 1981.

[19] SKF group. Bearing damage and failure analysis. https://www.skf.com/binaries/pub12/Images/0901d1968064c148-Bearing-failures---14219_2-EN_tcm_12-297619.pdf, 2017.

[20] JP. Jing, Y. Sun, SB. Xia, and GT. Feng. A continuum damage mechanics model on low cycle fatigue life assessment of steam turbine rotor. *International journal of pressure vessels and piping*, 78(1):59–64, 2001.

[21] M. Kaneta, Y. Murakami, and T. Okazaki. Growth Mechanism of Subsurface Crack Due to Hertzian Contact. *Journal of Tribology*, 108(1):134–139, 01 1986.

[22] A. Karolczuk. Non-local area approach to fatigue life evaluation under combined reversed bending and torsion. *International Journal of Fatigue*, 30(10-11):1985–1996, 2008.

[23] N. Kihlström. Big bearings boost offshore pipe laying. https://www.skf.com/group/news-and-events/news/2020/2020-08-20-big-bearings-boost-offshore-pipe-laying, 2020.

[24] J Lemaitre. *A course on damage mechanics*. Springer Science & Business Media, 2012.

[25] GH. Li, Y. Jiao, and ZW. Wu. Defect diagnosis of low-speed heavy-duty bearings using acoustic emission. In *World Conference on Acoustic Emission*, pages 249–257. Springer, 2017.

[26] P. Lotfollah and G. Blacquière. Fatigue crack sizing in steel bridge decks using ultrasonic guided waves. *Ndt & E International*, 77:49–62, 2016.

[27] KT. Ma, Y. Luo, and CTT. Kwan. *Mooring System Engineering for Offshore Structures*. Gulf Professional Publishing, 2019.

[28] S. Mateusz. Fatigue model choose. https://www.comsol.com/blogs/fatigue-model-choose/, 2014.

[29] B. Mattoso. FPSO Turret System - Bearing Issues. https://www.linkedin.com/pulse/fpso-turret-system-bearing-issues-bruno-mattoso/, 2018.

[30] ANSYS® Academic Research Mechanical. *Release 15.0, Help System, Mechanical APDL Material Reference*. ANSYS,Inc.

[31] MA. Meggiolaro and JTP. De Castro. Isotropic and kinematic hardening models for non-proportional multiaxial loading histories. *Tecnologia em Metalurgia, Materiais e Mineracao*, 20100726:1847–1858, 2010.

[32] SM. Moghaddam, F. Sadeghi, K. Paulson, N. Weinzapfel, M. Correns, V. Bakolas, and M. Dinkel. Effect of non-metallic inclusions on butterfly wing initiation, crack formation, and spall geometry in bearing steels. *International Journal of Fatigue*, 80:203–215, 2015.

[33] GD. Nguyen, AM. Korsunsky, and JPH. Belnoue. A nonlocal coupled damage-plasticity model for the analysis of ductile failure. *International Journal of Plasticity*, 64:56–75, 2015.

[34] A. Niesłony. Determination of fragments of multiaxial service loading strongly influencing the fatigue of machine components. *Mechanical systems and signal processing*, 23(8):2712–2721, 2009.

[35] J. Oliver, A.E. Huespe, M.D.G. Pulido, and E. Chaves. From continuum mechanics to fracture mechanics: the strong discontinuity approach. *Engineering fracture mechanics*, 69(2):113–136, 2002.

[36] AV. Olver. The mechanism of rolling contact fatigue: an update. *Proceedings of the Institution of Mechanical Engineers, Part J: Journal of Engineering Tribology*, 219(5):313–330, 2005.

[37] R.Basan, M.Franulović, I.Prebil, and R.Kunc. Study on ramberg-osgood and chaboche models for 42crmo4 steel and some approximations. *Journal of Constructional Steel Research*, 136:65–74, 2017.

[38] J. Schijve. *Fatigue of structures and materials*. Springer Science & Business Media, 2001.

[39] S.Commend and T. Zimmermann. Object-oriented nonlinear finite element programming: a primer. *Advances in Engineering Software*, 32(8):611–628, 2001.

[40] J. Skrzypek and A.Ganczarski. *Modeling of material damage and failure of structures: theory and applications*. Springer Science & Business Media, 1999.

[41] S.Murakami. *Continuum damage mechanics: a continuum mechanics approach to the analysis of damage and fracture*, volume 185. Springer Science & Business Media, 2012.

[42] R. swarbrick. Yield surfaces. `https://en.wikipedia.org/wiki/Von_Mises_yield_criterion#/media/File:Yield_surfaces.svg`, 2017.

[43] NB. Thomsen and BL. Karihaloo. Subsurface and surface cracks under contact loading in transformation-toughened ceramics. *Journal of the Mechanics and Physics of Solids*, 44(2): 207–231, 1996.

[44] RK. Upadhyay and LK. Kumaraswamidhas. Bearing failure issues and corrective measures through surface engineering. In *Handbook of Materials Failure Analysis*, pages 209–233. Elsevier, 2018.

[45] W.Caesarendra, B.Kosasih, A.Tieu, HT. Zhu, C. Moodie, and Q. Zhu. Acoustic emission-based condition monitoring methods: Review and application for low speed slew bearing. *Mechanical Systems and Signal Processing*, 72:134–159, 2016.

[46] Y.Yin, YX.Chen, and L. Liu. Lifetime prediction for the subsurface crack propagation using three-dimensional dynamic fea model. *Mechanical Systems and Signal Processing*, 87:54–70, 2017.

[47] ZL.Mo, JY. Wang, H. Zhang, XF. Zeng, HY. Liu, and Q. Miao. Vibration and acoustics emission based methods in low-speed bearing condition monitoring. In *2018 Prognostics and System Health Management Conference (PHM-Chongqing)*, pages 871–875. IEEE, 2018.

[48] M. Žvokelj, S.Zupan, and I. Prebil. Multivariate and multiscale monitoring of large-size low-speed bearings using ensemble empirical mode decomposition method combined with principal component analysis. *Mechanical Systems and Signal Processing*, 24(4):1049–1067, 2010.

A

Validation

This part is aimed to show the validation with other paper. The dynamic transient analysis is used in Feishen et al [17], and friction parameters are also included. Additionally, the elastic strain coupled with damage mechanism is also considered. Figure A.1 shows the results of stress variation within the first cycle by Feishen et al [17].

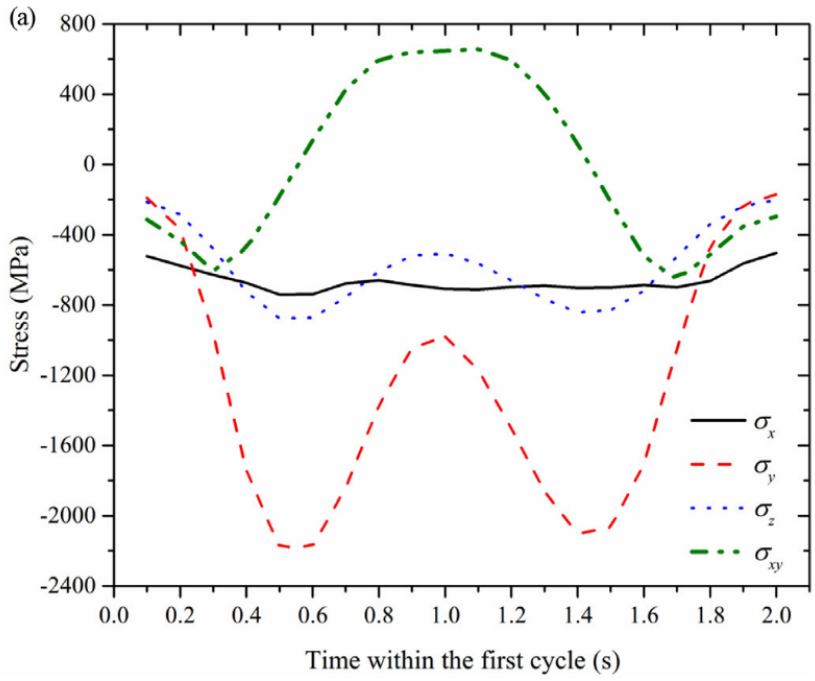

Figure A.1: History of the stress components at the potential point within the first cycle [17]

The material choice in the locally coupled method is also shown in the following table.

Table A.1: The material parameters for AISI 52100 [17]

E(MPa)	v	σ_Y(MPa)	R_∞(MPa)	b	c_1(MPa)	c_2(MPa)	γ_1	γ_2	S(MPa)
152,000	0.3	1500	315.87	56.09	593,303	4788.5	1000	55.9	100

The following table is the comparison of life estimation based on the locally coupled method and Feishen et al [17]. The observed 25% difference between this research and Shenfei et al is acceptable since both values are at the same order magnitude despite the significant differences in the approaches.

The elastic strain is also considered in Feishen et al [17] due to the loading condition and material. In this research, since the elastic amplitude is small compared with plastic strain, the damage evolution due to elastic strain is reasonably ignored.

Table A.2: The comparison of life estimation based on the locally coupled method and Feishen et al [17].

Locally-coupled method	Feishen et al (only plastic strain considered)
5.1×10^5	6.8×10^5

B

Further study

Following the results from the numerical study, this section is to discuss the further study of the monitoring methods. In monitoring methods, for large scale low-speed roller bearing, damage detection is very difficult compared with high-speed roller bearings. This is because in low-speed roller bearings, in noise environment for example when the roller is in operation, the errors due to the background noise can not be avoided. Another reason is the wide range of high frequencies due to the slow speed. Considering both reasons, the classical method like vibration analysis is not used in this research, meanwhile, AE method is used to detect the damage state of the defected roller bearing. In this section, there remain two parts-fatigue experiment which is in process under HiTeAM, and application which is discussed about the combination of the numerical method and monitoring.

B.0.1. Fatigue experiments

For low-speed roller bearings, its diameter is normally large in heavily-loaded condition and it is expensive to make the same scale in lab test. Furthermore, the production of such bearing takes long time cause normally they need to be customized in professional factory instead of mass production. The simplification of such roller bearing should be considered. For this reason, as the curve of large scale of raceway of roller bearing is infinite. This large scale roller bearing can be simplified by rollers move between two flat plates.

The following figures are the schematic about a double bearing arrangement of HiTeAM JIP, so as to simulate and study the damage state under the actual operation condition of turret or slew bearing.

This test set-up consist of a 24 channel AMSY-6 Acoustic Emission measurement system with ASIP2/A signal processing cards are mounted on the raceway. These 24 sensors are situated in the 8 locations as 3 sensors in each location (See right in the figure B.1). These three sensors are separately an R6α 60 kHz resonant AE transducer, an R15α 150 kHz resonant AE transducer, and a WSα broadband (>200 kHz) AE transducer. All sensors are pre-amplified applying AEP-5H AE preamplifiers as a set up gain of 40 dB. Loctite 480 super glue are used for the attachement of sensors and raceway.

A load of 1300 kN will be imposed vertically using a hydraulic cylinder. A horizontal cylinder will control the movement of rollers by pushing and pulling on the nose ring with a total stroke length of 70 mm in 12 seconds so as to make sure the speed of rollers is constant at 11.67 m/s. The vertical and horizontal cylinder pressure (load) and displacement are logged by SCADA.

As shown in figure B.1, four main parts are shown: support ring (light blue), top roller -raceway, bottom roller-raceway (yellow and dark blue parts), and nose ring (green) between top and bottom roller-raceway.

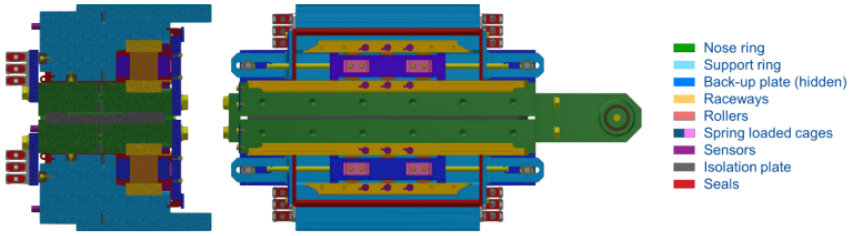

Figure 1: Test set-up front view (left), and side view (right)

Figure B.1: Test set-up front view, and side view (right) [7]

B.0.2. Application

The crack size and crack locations can be detected by this lab test, although the detection range may be limited. This is because when crack is short especially in noisy environment like operational case, the background noise can mask the basic information of short crack. Meanwhile, from the numerical results, this minimum detection length in our case should be at least 10mm.

A comparison between numerical results and experiment for intact model is proposed. The numerical condition is ideal but in practise, there remain a lot of influence factors such as corrosion, non-mental inclusions and friction. Furthermore, considering the acceptable error tolerance due to the complex fatigue process, the numerical results can give a rough estimation on the remaining life once the first AE sensors detected. For example, if the first AE sensor get the damage state is 12.5mm at the depth of 5mm under raceway, then, the rough estimation is 1000-1400 cycles. For the exact estimation, the numerical results should be validated by the monitoring results.